Experimental Validation of Solar Photovoltaic and Battery Storage-Based Microgrid Energy Management System

By
Rupak Kanti Dhar

A Thesis Submitted to
Saint Mary's University, Halifax, Nova Scotia
in Partial Fulfillment of the Requirements for
the Degree of Master of Science in Applied Science.

October 13, 2020, Halifax, Nova Scotia

Approved: Dr. Adel Merabet
Supervisor
Division of Engineering,
Saint Mary's University

Approved: Dr. Amer M. Y. M. Ghias
Supervisory Committee
School of Electrical and Electronic Engineering
Nanyang Technological University
Singapore

Approved: Dr. Hamed Aly
Supervisory Committee
Department of Electrical and Computer Engineering
Dalhousie University, Halifax, NS

Approved: Dr. Andrew Swingler
External Examiner
Department of Sustainable Design Engineering
University of Prince Edward Island, Charlottetown, PEI

Date: October 13, 2020

Experimental Validation of Solar Photovoltaic and Battery Storage-Based Microgrid Energy Management System

by Rupak Kanti Dhar

Abstract

The purpose of this work is to design and implementation of an energy management system for a solar Photovoltaic (PV) and battery storage-based microgrid system. The control architecture of PV, battery, and inverter units are presented here. A rule-based energy management system is proposed by considering some crucial factors such as, battery capacity, economical operation, profit-making, utility billing, efficiency etc. The seamless operation of the microgrid has been achieved for grid-connected and islanded condition. A set of power electronics interfaces, based on various converters and inverters, are used to integrate solar PV and battery storage to the DC-bus. Optimal power exchange between the main grid and microgrid unit is ensured, while power balance is achieved in every cases. In addition, Water Cycle algorithm (WCA) is employed for PI parameters optimization rather using conventional trail-error tuning method. The proposed EMS and control scheme are implemented using Festo-LabVolt and real-time Opal-RT interfaces. Experimental results demonstrate the accuracy and robustness of the proposed microgrid energy management system under different operating conditions.

October 13, 2020

Table of Contents

List of Tables

List of Figures

Acknowledgement

In the first place, I would like to thank Saint Mary's University, Halifax, Canada, for providing me the opportunity to pursue the M. Sc. in Applied Science program with funding and research fellowship. My sincere thanks also go to Canada Foundation of Innovation for the Grant (Grant# 30527), Faculty of Graduate Studies and Research, and Government of Nova Scotia for Nova Scotia Graduate Scholarship.

I would like to express my deepest gratitude to my supervisor Dr. Adel Merabet for his diligent guidance, motivation, and patience all through the research work. Beside my supervisor, I would like to thank my supervisory committee members Dr. A. M. Y. Mohammad Ghias and Dr. Hamed Aly, for their encouragement and valuable comments.

I would also like to thank the entire research group of Laboratory of Control Systems and Mechatronics and Division of Engineering at Saint Mary's University for their support and help.

Finally, I am indebted to my parents and family members for their hard-work, wisdom, encouragement, and limitless sacrifices.

October 13, 2020

List of Abbreviation

Acronyms	Description
PV	Photovoltaics
MPPT	Maximum Power Point Tracker
EMS	Energy Management System
DG	Distributed Generation
RES	Renewable Energy Sources
VSI	Voltage Source Inverter
PWM	Pulse-Width Modulation
LPF	Low Pass Filter
IGBT	Insulated-Gate Bipolar Transistor
PI	Proportional Integral
FLC	Fuzzy Logic Controller
ANN	Artificial Neural Networks
AI	Artificial Intelligence
PCC	Point of Common Coupling
THD	Total Harmonic Distortion
WCA	Water Cycle Algorithm
GA	Genetic Algorithm
HIL	Hardware-In-The-Loop
SOC	State of Charge
DRTS	Digital Real-Time Simulation
PPPE	Photovoltaic Power Profile Emulator
FPGA	Field Programmable Gate Array

Chapter 1: Introduction

1.1 Introduction:

A microgrid is a localized group of electricity sources and loads capable of operating in parallel with, or independently from, the main power grid. It is a discrete energy system which includes generation, storage, demand management, and loads, normally operates connected to a synchronous grid (main-grid), but can also disconnect to islanded mode and function autonomously as physical or economic conditions dictate [1], [2]. The primary purpose is to ensure reliable, and affordable energy security for rural and urban communities, while also providing solutions for commercial, industrial, and federal government consumers. A microgrid can effectively integrate various sources of DG, especially RES - renewable electricity, and can supply emergency power, changing between island and connected modes [3], [4]. In many respects, microgrids are miniature versions of the traditional power grid which have several units such as, power generation and distribution unit, variable load, and control units such as voltage regulation, frequency control, current control etc. Circuit breakers, fuses, contractor are the commonly used switchgear and protection devices in microgrid. Despite of the likeliness, microgrids differ from traditional grids by providing a closer proximity between power generation and power use. Microgrids also integrate with renewable energy sources such as solar PV, wind power, small hydro, geothermal, waste-to-energy, and combined heat and power (CHP) systems [3]-[5].

An overview of microgrid system is depicted in Figure 1.1. Microgrid performs several tasks such as, interoperate with existing power systems, dynamic control over energy sources, enabling autonomous and automatic self-healing operations, network infrastructure, information systems, and power back to the main-grid during power outages [5]. Following features can be summarized for the microgrid technology:

- Provides power reliability for consumer and owner.
- Enhances the integration of distributed and renewable energy sources.
- Economical and profit-making is possible.
- Building blocks for a complete smart-grid.
- Power control can be both locally and centrally.

- Clean energy generation and minimizing carbon emission.
- Both consumer and owner can participate in the energy market.

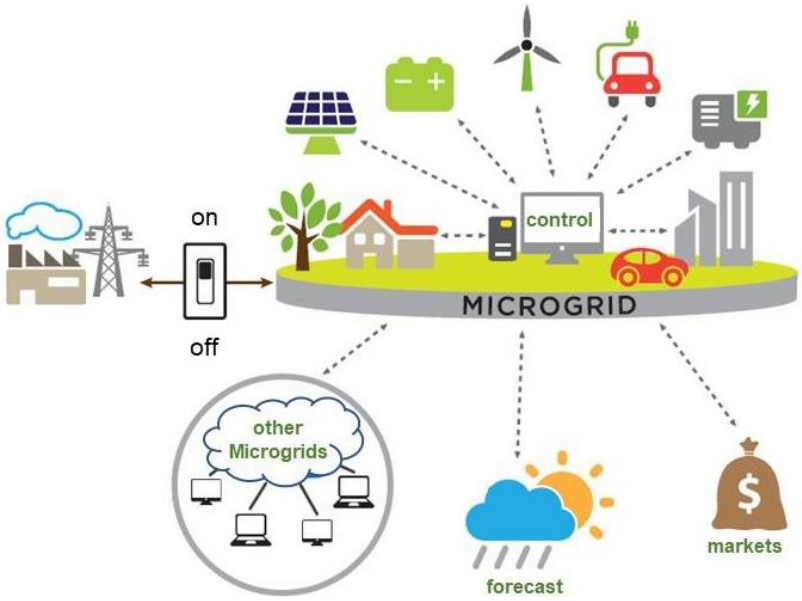

Figure 1.1: Overview of a microgrid system [5].

1.2 Background Study:

The Last two decades have been witnessed an abundance of microgrid systems. Despite the advantages, some challenges in the area of integration, control, and energy management, yet to be explored. Hence, the scope of improvement in the existing ideas draws great attention from researchers and engineers. In this section, some prior studies reported in the literature have been discussed.

1.2.1 Classification of Microgrid Control:

Various microgrid configurations in structure and control topologies are possible to implement. Some common microgrids are military and ship base microgrid, remote off-grid microgrid, residential and commercial microgrid, community and campus-based microgrid, etc. Other types of microgrids, for instance, an active distribution system (ADS), cognitive microgrid, and virtual power plant (VPP) [6] – [8], are building blocks for smart grid application. The hierarchy of microgrid control is depicted in Figure 1.2. While dealing with microgrid the control

units must ensure some factors such as [9]-[11], response time, accuracy, communications protocol, etc. The hierarchical control levels can be classified into three major sections: primary control, secondary control, and tertiary control.

Firstly, primary control is the local control which is the fastest and requires no communications. Power-sharing control, VSI control, frequency control, are performed at the primary control level. In the inverter control voltage regulation and current control are generally controlled when the system is grid-connected, however, frequency control is required in islanded microgrid [12]-[14]. For power-sharing two approaches are taken: droop-based method and non-droop-based method. The imbalance of power between the generator and load is solved by considering a frequency deviation. There are many advanced droop approaches such as fuzzy-based droop, adaptive-droop, ANN-based droop, which are already studied in different projects. In the non-droop primary control approach, controllers get signals from the central controller. Master-slave, CANbus are some common control approaches in the non-droop method [14].

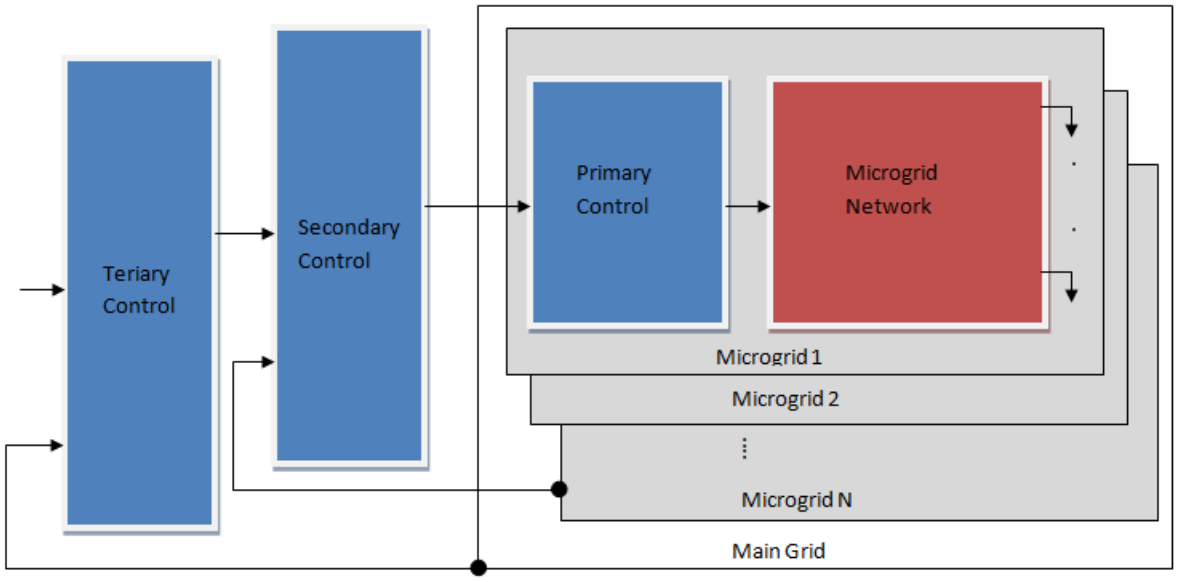

Figure 1.2: Hierarchical control levels [13].

The next control level is the secondary control, which is generally referred to as the EMS. The cost-effective and optimal functions are ensured in this control stage. Basically, outputs of secondary control happen to be the input for primary control. Although there is a tertiary level, secondary level control is considered the highest level of control in a stand-alone or islanded

microgrid. There are two types of a control architecture for secondary control: Centralized approach and decentralized approach. The centralized controller can make decisions using either online calculations of the optimal (or near-optimal) operation as it is provided with all information of the network parameters, such as forecasting of load, wind speed, solar irradiance, utility price, profit-making [13]-[18], etc. On contrary, a decentralized secondary control intends to solve the EMS problem by providing commands to local units [17]-[20]. It interacts with higher-level controllers and trying to achieve local and global objectives. Finally, tertiary control is the highest level of control interact with the power grid. It is also responsible for coordinating and interconnection among multiple microgrids. The reactive power injection can be ensured in the point of common coupling (PCC) by the tertiary level control [16], [19].

1.2.1 Trends in Energy Management System:

According to the PCC, a microgrid can be DC-bus, AC-bus, or hybrid configuration. Due to the wide range of DC power sources in microgrids such as PV, fuel cell, and energy storage, DC-bus microgrid has been used in many projects. Alongside, AC-bus microgrid has been an area of interest for traditional AC power systems. Both DC and AC-bus microgrid has some pros and cons. As a matter of fact, recently hybrid AC/DC microgrids became more popular. Although controls in hybrid AC/DC are quite complex, the most possible future distribution and transmission systems would be in hybrid architectures. It is noteworthy that, likely to AC or DC microgrids, hybrid microgrids can operate both in grid-connected and stand-alone mode [20].

Microgrids offer several advantages such as a reduction in carbon emissions, reactive power injection, supply-demand balance, economic operations, etc. However, it has numerous operational challenges that need to be addressed in EMS and control design. The constraints can arise from distribution, transmission, control, and prediction units [20]-[23]. Due to voltage mismatch and fault in the protective device, bidirectional power flow can be interrupted. Control units happen to be vulnerable to the stability issues. Instability occurs in many cases, among them local oscillation and transition from off-grid to grid-connected are the most common phenomenon [5],[20]. Low inertia characteristic makes disunity while exchanging power with high-inertia synchronous generators. Another significant constraint in a microgrid is uncertainty. The load profile and the weather are the two most common uncertainties that make the system more challenging [22], [23].

The design of EMS must consider these constraints; however, no EMS model can aggregate all these constraints. The benefits of EMS include but are not limited to reliability, energy balance, customer privacy, cost degradation. Different researches have been conducted in Asia, Europe, and America [24]-[38], which introduce tremendous EMS techniques.

Linear and nonlinear programming methods find the optimal solution for the EMS. Linear programming is an important concept in optimization techniques in mathematics as it helps to find the most optimized solution to a given problem. On the other hand, nonlinear programming is the mathematical method of finding the optimized solution by considering constraints or objective functions that are nonlinear [30]-[32]. The dynamic rule-based energy management algorithms are dominated in the industry due to their fast computation and ease of establishment potentials, however, their performance differs a lot from the improper setting of parameters and control actions [33], [34].

In case of solving EMS problems, meta-heuristic is a higher-level procedure to find or select a heuristic (partial search algorithm) that may provide a sufficiently good solution to an optimization problem, especially with incomplete or imperfect information or limited computation capacity. Genetic, swarm practical, WCA, random variable, are some globally recognized heuristic method for EMS optimization [35]. In many reports [33]-[37], artificial intelligence such as FLC and ANN, have been used in EMS for smooth power-sharing, fluctuation reduction, and cost minimalization purpose. Multi-agent-based EMS is an advanced software-based technology used for making models manage data. The software agent created acts like a human (agent) to do anything automatically according to the present conditions. Agents have the ability to think and analyze by themselves. The decentralized approach is mostly used in multi-agent-based EMS as the consumers, storage units, generation units, and grid are considered as agents [35], [37]. In a learning-based predictive EMS model, loads and demand are calculated for predictive control which is combined with weather prediction models operated by a model predictive controller to forecast supplied energy [36]-[39].

There are other EMS techniques available for EMS modeling. The aforementioned EMS have their significances for a particular application; however, every EMS model has some limitations.

1.2.2 Experimental and Real-World Microgrids:

A redundant of EMS models have been proposed and implemented in simulation platforms. For the present power electronic and power system infrastructures, many EMSs are still unfeasible to implement in the real-world. Even though, some EMS can be proved unimplementable in the laboratory as well. The following discussion is all about the study of the real-world microgrid on a commercial and laboratory-scale.

In Canada, the BC Hydro Boston Bar and Hydro Quebec (HQ), Canada are two prominent microgrid systems. Boston Bar is a 8MW, 69 kV microgrid, whereas Hydro Quebec (HQ) is 120KV, 7MW configuration [40], [41]. The CERTS testbed is a full-scale testbed built near Columbus, Ohio, and operated by American Electric Power. It's a three-feeder system of 60 kW each. Here, each generator set is provided with battery energy storage at its DC bus [42]. Bronsbergen Holiday Park microgrid is supported by the European Union. consists of 208-holiday homes. The microgrid is formed in the park and the generation comes from 108 roofs fitted with solar PVs and the peak generation capacity is 315 kW [43]. The Residential Microgrid of Am Steinweg in Stutensee –German is built to test the work carried under the DISPOWER project. Am Steinweg microgrid is a three-phase low voltage (400 V) four-wire system, which is connected to the medium voltage (20 kV) network through a 400 kVA transformer.

UW microgrid testbed at the University of Wisconsin – Madison is implemented to investigate the modeling and control issues in integrating diesel generators into microgrids that can also include convertor-based sources [42]. Laboratory-scale microgrid system at National Technical University of Athens (NTUA) – Greece, operates in parallel to the grid, the inverter follows the grid. The system is built on the Java Agent Development Framework (Jade) 3.0 platform; thus, the communication language could be either XML or SL [44]. University of Manchester microgrid/flywheel energy storage laboratory prototype – the UK, rated at 20 kVA. The flywheel is 100 kW unit down rated to 20 kW power output. A three-phase balanced load of 12 kW is connected at the end of the feeder. The 0.4 kV mains supply of the laboratory is considered as the main grid. Kyoto eco-energy project (Kyotango project) – Japan, carried out under NEDO projects. The microgrid is formed by a plant having gas engines with a total capacity of 400 kW, a 250 kW MCFC and a 100-kW lead-acid battery, and two PV systems and a 50-kW small wind turbine connected at remote locations [45]. Another Test network, at Akagi of the Central Research

Institute of Electric Power Industry (CRIEPI) – Japan, is aimed to evaluate new test equipment under integrated control [46]. Test microgrid at the Institution of Engineering and Technology – India, consists of two PSObased inverters fed from fuel cell stacks, sine PWM inverter connected to an uncontrolled rectifier fed from a DC motor-driven induction generator (2.2 kW, 415 V, 50 Hz, three-phase, 0.85 p.f. and the rotor is of squirrel cage type). The grid capacity considered for the experimental set-up is 3.2 kVA, 415 V, three-phase, and 50 Hz [47].

1.3 Literature Review and Motivation:

Researchers have investigated different microgrid and EMS via simulation and experimental tests. Microgrid research has a significant share of advancement, however, some gaps in prior work are still to be addressed. In [48], [49], a single-stage grid-connected PV microgrid with MPPT is discussed. Although the system reflects efficiency, battery size, and cost, the current compensation and %THD are not presented. Similar microgrids have been analyzed in [50], [51], however, they are two-stage rather than single-stage. In [52] and [53], a typical distributed control strategy is applied to dc microgrid where AC-bus determines the converter actions. Here, for over-voltage and over-current conditions storage device needs to be well modeled for safety purpose. Regardless of the priority and sequential adding of sources, in [54] islanded-mode and grid-connected mode of microgrid have been discussed considering voltage and frequency control.

In [55], [56], an advanced fuzzy system such as multi-mode fuzzy and adaptive fuzzy logic, are used for EMS design. Despite being an intelligent system, fuzzy systems are error sensitive in simulation and experimental platforms. In [57], ANN-based EMS has been designed considering SOC states, however, ANN involves complex computation in real-time systems. The studies presented in [58], [59] discussed power-sharing on the generating and demand side. Better performances have been demonstrated; however, the system may stress the battery life. Mixed Integer Non-Linear Programming (MINLP) optimization is introduced in [60] for islanded microgrid, where equations are linearized using piece-wise functions. But this optimization technique is computationally challenging and not completely suitable for online applications.

Many studies have been reported on microgrid robust control applications in [61]-[65]. In the context of optimal sizing and reconfiguration of hybrid microgrid, [61] used a Genetic algorithm (GA) taking weather and annual cost into account. Similar research has been conducted in [62],

where Particle Swarm Optimization (PSO) is compared with GA. Related research in [63]–[65] have been applied to microgrids voltage and frequency stability, and cost reduction. However, stuck in local optima is a common phenomenon that happens generally in PSO-based multi-objective models. In [65], GA-based-MES is proposed for cost minimization, although the convergence problem is not solved yet.

Some noteworthy researches have conducted in [66]-[72], for laboratory-scale DC-bus microgrid. In these aforementioned articles, working EMS and PI and hysteresis-based control are implemented. Despite proper functioning test-bed, the addressed system used conventional PI rather than using any optimization techniques.

1.4 Objective and Contribution:

From the background study and literature review, an overall idea on advancement in microgrid research can be comprehended. Studies in [48]-[60] generalize the microgrid power balance and sharing, and the cost minimization. In addition, different EMS for the optimal operation has been demonstrated. The visions of the researchers are quite impressive for the future smart grid. However, most of the ideas are yet to be implemented for experimental tests. As we know AI or algorithm-based computational time is higher and sometimes difficult for physical implantations. Moreover, local minima and inappropriate convergence happen to be a matter of concern for this kind of system. The reports from [40]-[42], are some real-world microgrid where basic EMS has been applied. In [45], [67], [68], [69], tremendous laboratory-scale microgrid experiment is carried out. In the papers, controller parameters are optimized only by trail-error tuning, which is a tiresome and time-consuming technique. Besides, some experiment has been done only in HIL environment [71], [72].

The main purpose of this research work is to design and experimentally validate a DC-link microgrid, where factors and constraints such as efficiency, battery capacity, and battery life, cost reduction, financial benefits, have been taken under consideration. The main objectives and contribution of this work are as follows:

- Design and implement of a solar PV and battery-based DC-link microgrid. A decentralized control approach has opted. In addition, the microgrid is capable of working in grid-connected and islanded mode operation.

- Develop and test, a rule-based EMS for microgrid optimal operation. Moreover, ensuring the seamless operation during the transition between operating modes.
- Applying WCA instead of conventional trail-error tuning for the PI controller parameters optimization.
- Experimental validation of the prosed microgrid control and EMS.

1.6 Outlines:

The thesis work is presented in six chapters. The rest of the chapters are organized as follows:

Chapter 2 talks about the detail modeling of the microgrid controllers. All the theory and mathematical formulation are introduced here.

Chapter 3 proposes the EMS for the microgrid. The operating principle for each case in the EMS is elaborated in this chapter.

Chapter 4 describes digital real-time simulation and communication protocols. A brief description of Opal-RT interfaces and RT-Lab technology is discussed. In addition, brief elaboration on, LabVolt physical inverters and power electronics components are given.

Chapter 5 is the validation of the research. In this chapter, the experimental results from the microgrid are given and observed for the proposed EMS.

Chapter 6 tells us about the future scope of the work. And finally, this chapter concludes and summarize the research project.

Chapter 2: Microgrid Control Architecture

2.1 Introduction:

Solar PV is the most popular and widely used distributed generation (DG) due to its low installation cost and arability of irradiance. Common generating units such as solar DC, storage device, fuel cell, are DC power sources, so DC-bus microgrid is exceedingly preferable and compatible with power system integration. On the other hand, AC-bus or hybrid configurations are more complicated and require more power electronic components [5], [66]. In this research project, a PV and BS-based small-scale grid-connected DC-microgrid is designed and implemented. The proposed microgrid is depicted in Figure 2.1. For any renewable technology storage device is required while any energy management is taking place. In this work, lead-acid based battery storage is connected to the DC-side of the inverter through a buck-boost converter. Similarly, the solar PV is delivering power through a boost converter to the inverter. The necessity of the boost and buck-boost converter is to ensure the output voltage of the converters to be exactly stepped up or down to the DC-link voltage.

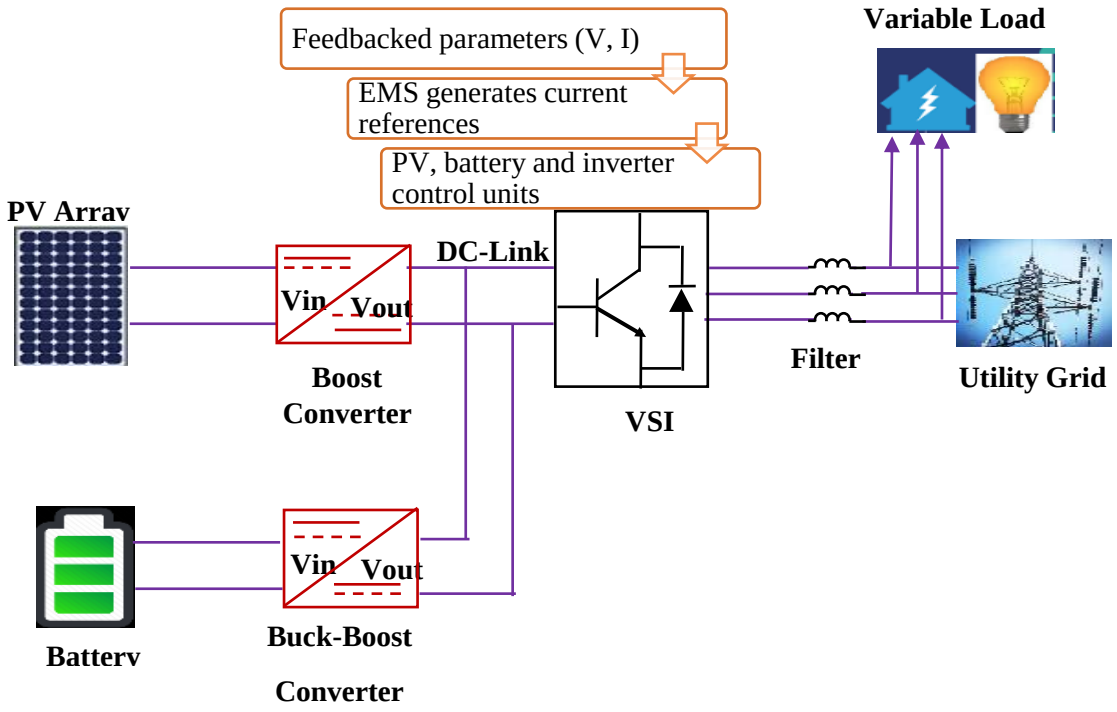

Figure 2.1: Schematic of PV and BES-based microgrid.

In ideal case power before and after the converter should be the same, however, in practice, it is quite impossible. The proposed microgrid is a grid-connected system where the grid taking cake of the voltage and frequency of the AC-side. The VSI is the heart of the system as it is inverting the DC to AC. A variable load is connected in the AC-side to demonstrate the power balances in different. The aforementioned microgrid is consist of three major control unit: PV local control; BS local control and grid-connected VSI control. A decentralized control technique has been adopted for communication between EMS and local control units. Moreover, the optimization of the PI controller parameter is performed using the water cycle algorithm (WCA) rather than applying the trail-error method. A detailed discussion of the controller design is presented in the succeeding sections.

2.2 Solar PV Local Control:

A solar cell consists of layers of semiconductor materials that exploit the photoelectric effect of converting photon energy of the solar radiation into electricity [73], [77]. It can be considered as a nonlinear current source [80]. The IV curve of PV array is depicted in Figure 2.2, where the relation between PV current and voltage can be easily deduced. In addition, the power changes in array with the change of PV voltage can also be observed. MPPT is the point in a PV array where the maximum amount of power is extracted from the solar irradiance.

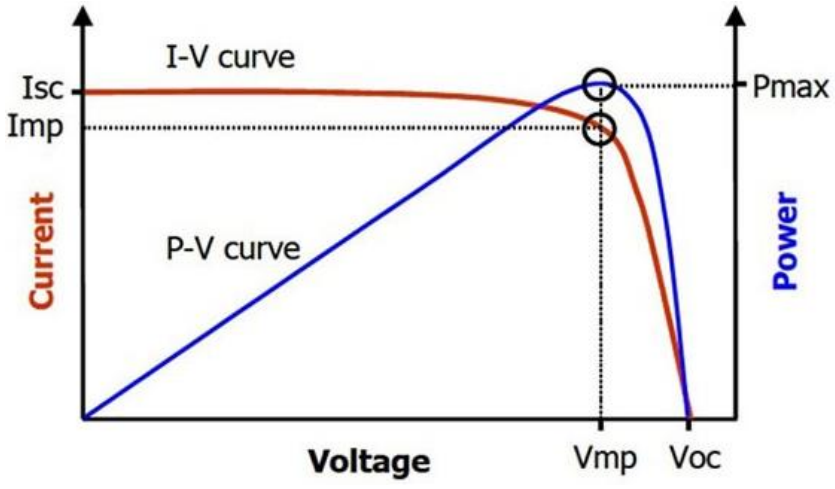

Figure 2.2: IV curve of a PV array [75].

The equivalent circuit for a PV array is presented in Figure 2.3, which is modeled using the I-V relationship of a PV cell such as [73]-[78].

$$I_{PV}=N_pI_r-N_pI_0\left[exp\left(\frac{q(V_{PV}+N_sR_sI_{PV})}{N_snkT}\right)-1\right]-\frac{V_{PV}+\frac{N_s}{N_p}R_sI_{PV}}{\frac{N_s}{N_p}R_p} \quad (2.1)$$

where T is the cell temperature, q is the electronic charge, k is the Boltzmann constant, n is the ideality factor, I_{pv} and $V_{pv}$are the current and voltage outputs of the PV array, I_r is the irradiance current, I_0 is the diode saturation current, R_s is the series resistance, R_p is the shunt resistance,

$N_s = N_m \times N_c$ ($N_m$is the number of panels connected in series in the array and N_c the number of cells connected in series in the panel respectively. The irradiance current, I_r is given by,

$$I_r=I_{r,STC}\left(\frac{G}{G_{STC}}\right)[1+\alpha_T(T-T_{STC})] \quad (2.2)$$

$$P_{PV}=V_{PV}I_{PV} \quad (2.3)$$

where, *GSTC* is the irradiance under *STC*, αT is the temperature coefficient of the short-circuit current, *STC* is the irradiance current under *STC* (Standard Test Conditions), G is the solar irradiance, P_{pv} is the PV power and T is the cell temperature.

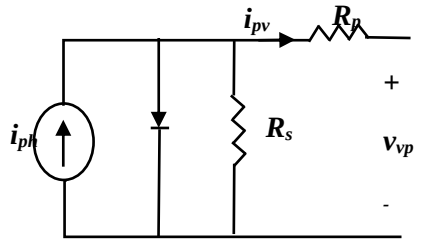

Figure 2.3: The equivalent circuit for a PV array [75].

Generally, DC-link is the distribution point, and it requires higher voltage for AC distribution, hence, the MPPT forces the boost converter to operate the PV at a lower voltage. There are several types of MPPT control techniques to improve solar energy efficiency such as, Incremental Conductance (INC), Hill Climbing or Perturbation and Observation (P&O), Artificial Neural Network (ANN) with backpropagation technique, Fuzzy Logic Controller Intelligent Control (FLCIC), etc. P&O algorithm has been extensively used due to ease of implementation as explained using flow charts provided in the Appendix. A.

In this work, a P&O algorithm-based MPPT is used to control the DC-DC boost converter. The algorithm compares the voltage and power of time (t) with the sample at time Δt and predicts the time to approach to MPP. The expression for the solar PV power and the MPPT algorithm power

variation is given by [76]-[80].

For the simplification here we are taking, $V_{PV}I_{PV} = VI$,

$$dP_{pv}=dVI+VdI \tag{2.4}$$

Here, V and I are the voltage and current at the terminals of PV panel, At MPPT, the power variation with respect to voltage becomes,

$$\frac{dPpv}{dV}=I+V\frac{dI}{dV}=0 \tag{2.5}$$

The discretization formula for Eq. (4) has considered from [70], which is given by,

$$dP_{pv}(t) \approx \Delta P_{pv}(kt) = \Delta V(k\Delta t)*I(k\Delta t) + V(k\Delta t)*\Delta I(k\Delta t) \tag{2.6}$$

The output voltage relation for the DC-DC boost converter can be found by,

$$V_{DC}=V_{PV}\left(\frac{1}{1-D}\right) \tag{2.7}$$

Here, and k, D are a positive integer and duty cycle respectively.

The control circuitry and control diagram are depicted in Figure 2.4, and in the control diagram, S_{d1} pulse is generated from the MPPT block to control the boost converter. A little voltage perturbation changes the power of the solar panel, if the power alteration is positive, voltage perturbation is continued on the same track. Conversely, if delta power is negative, it indicates that the MPP is far away and the perturbation is decreased to reach the MPP. Thus, in this way the whole PV curve is checked by small perturbations to find the MPP that increases the response time of the algorithm.

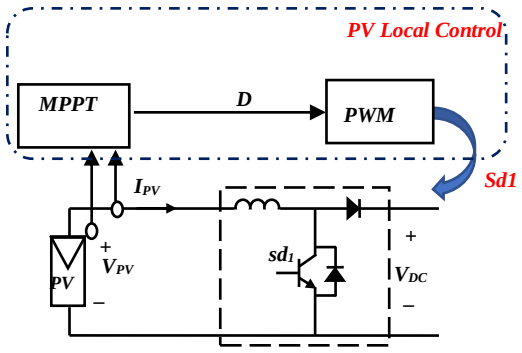

Figure 2.4: Solar PV local control

2.3 Battery Local Control:

There are various types of energy storage systems including battery, compressed air, flywheel, super-capacitor, fuel cell, pumped hydro, etc. the energy storage systems have their distinct advantages and limitations. A flywheel stores mechanical kinetic energy using a high accelerated flywheel to store energy and the flywheel is decelerated to discharge energy [78]. Compressed air uses air pressure to store energy by compressing air and release it when the load is high. A capacitor is an electrical device that stores energy in an electric field between a pair of conductors. Supercapacitor works in a similar way, but it has a higher energy density. A fuel cell converts the chemical energy in the fuel to electric current. Batteries are the most widely used form of energy storage which converts chemical and electrical energy to each other by chemical reaction. There are many different rechargeable batteries among them popular kinds are Nickel-Cadmium (Ni-Cd), Nickel-metal hydride (Ni-MH), Lead-Acid, and lithium-ion (Li-ion) batteries. Lead-acid batteries are the oldest but still popular rechargeable batteries. This battery technology uses lead and lead dioxide as electrodes and Sulphur acid as electrolyte [80]-[82]. Lead-acid batteries have deep discharge cycle durability and high discharge rates.

In this work, lead-acid battery storage is used and connected via a buck-boost converter to the DC-link of the microgrid. The main components in a buck-boost converter are much the same as in the buck and boost types, but they are configured in a different way. The adopted bidirectional DC/DC buck-boost converter is able to transfer energy between its two ports, supporting both positive and negative currents [82]. The relation between voltage and capacity in a battery storage is shown in Figure 2.5, where slight changes in battery cell voltage with change of capacity is observed. Until the minimum capacity, the voltage change is minimum, however, at zero capacity the cell voltage also becomes zero.

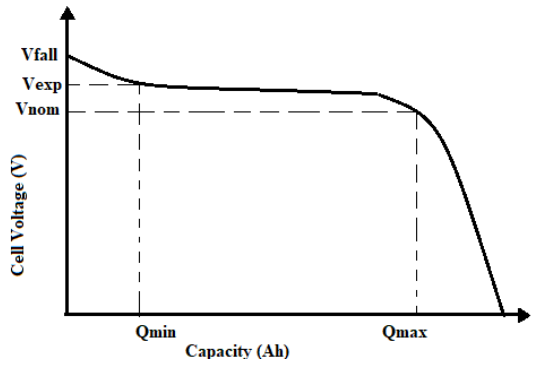

Figure 2.5: Relation between voltage and capacity in a battery storage [80].

The output voltage of the battery is given by [80],

$$V_{bat}=V_0-k\frac{Q}{Q-\int I_{bat}dt}+A\cdot exp(-B\int I_{bat}dt)-RI_{bat} \quad (2.8)$$

where, V_{bat} is the battery voltage, I_{bat} is the battery current, V_0 is the constant voltage capacity, $\int I_{\mathrm{bat}}dt$ is the extracted capacity, Q is the maximum battery capacity, k is the polarization constant, dt is the time step in hours, and R is the internal resistance, A is the exponential zone amplitude, B is the exponential zone time constant inverse. The battery power can be expressed as;

$$P_{bat}=V_{bat}I_{bat} \quad (2.8)$$

The actual battery capacity is represented by the SOC expressed by,

$$SOC(t)=SOC(t-1)+\frac{\int I_{bat}dt}{Q} \quad (2.9)$$

$$SOC_{min}\leq SOC\leq SOC_{max} \quad (2.10)$$

where, $SOC(t)$ is the battery state of charge at time t and $SOC\ (t-1)$ is the previous value of SOC. where, SOC_{min} and SOC_{max} are the minimum and the maximum allowable states based on the battery features.

Figure 2.6 shows the bidirectional boost-buck converter used to change the voltage from the input V_{bat}. Either the reference battery current can be generated from an EMS or it can be any fixed value provided by the user.

The voltage conversion ratio of a non-inverting buck-boost converter can be expressed as (2.11)

$$\frac{Vout}{Vin}=\left(\frac{D}{1-D}\right) \quad (2.11)$$

Where, D is the duty cycle. V_{in} and V_{out} are the battery voltage and DC-link voltage respectively.

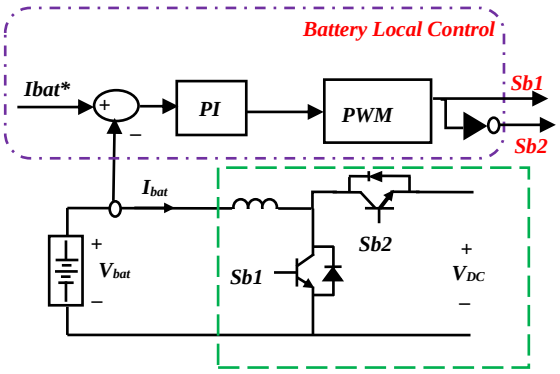

Figure 2.6: Buck-boost converter configuration for the BS.

The PI controller controls the battery current at the reference current and from the PWM the control signal is generated. The complementary pulsed Sb1 and Sb2 are used for boost and buck operation respectively.

2.4 Grid-Connected VSI Control:

In order to maintain constant DC-link voltage independent of the direction of power flow, a grid-connected VSI is used in this research. In inverter two control has been contracted: outer-loop DC-link voltage control and inner-loop current control. The DC-link is regulated by a PI controller whereas, the inner-loop current is controlled by the hysteresis controller. To avoid the computational complexity the hysteresis loop control is used. Although the control is a basic one, still it is globally accepted for its good range of performance. The configuration of VSI is shown in Figure 2.7. The inverter is grid-connected; hence the voltage and frequency are taken from the grid in the control unit. So, the voltage and frequency remain the same as the grid, however, only DC-link voltage and current flow is control in the inverter control.

The DC-link voltage error is given [79]-[80];

$$e=V_{dc}^{*}-V_{dc} \tag{2.11}$$

Where, V_{dc} and V_{dc}^{*} are the actual DC-link voltage and reference DC-link voltage respectively. i_v is the current at the inverter input, and C is the capacitance. The DC-link voltage dynamics is expressed, at the capacitor link illustrated in Figure 2.5, by

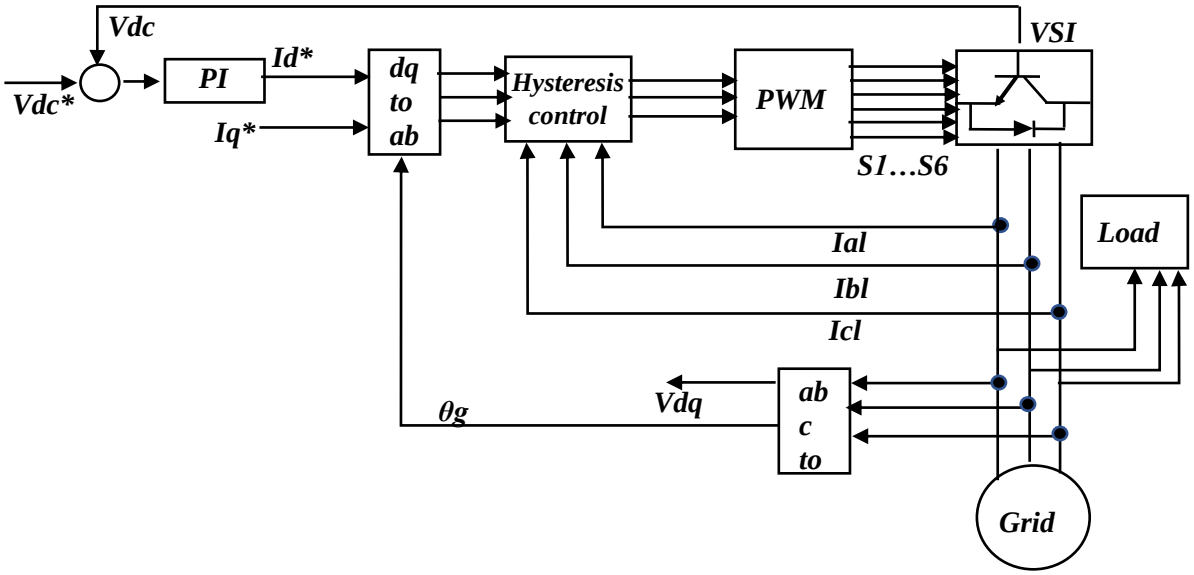

Figure 2.7: Grid-connected inverter control configuration.

$$C\frac{dV_{dc}}{dt}=\left((1-u_d)i_{PV}+(1-u_b)i_L\right)-i_v \quad (2.12)$$

The power, at the input of the inverter, is given by

$$P_v=V_{dc}i_v \quad (2.13)$$

The voltage components at grid-side in the dq frame are given by;

$$v_d=-Ri_d-L\frac{di_d}{dt}+L\omega i_q+v_{dl} \quad (2.14)$$

$$v_q=-Ri_q-L\frac{di_q}{dt}+L\omega i_d+v_{ql} \quad (2.15)$$

v_{dl} and v_{ql} respectively stand for the d and q-axis components of line voltage. i_{pv} inverter input current. Similarly, i_d and i_q respectively stand for the d and q-axis components of line current. Moreover, R and L are the filter resistance and inductance. The power at the inverter output, under the assumption of the voltage alignment ($v_q = 0$), is expressed by [20]

$$\begin{cases} P=3v_{dl}i_d \\ Q=3v_{dl}i_q \end{cases} \quad (2.16)$$

From (2.16) and (2.13), under the assumption of power lossless inverter, the inverter input-output powers are equal ($P_v = P$) and the current i_v can be expressed by

$$i_v=\frac{3v_d}{V_{dc}}i_d \quad (2.17)$$

By substituting (2.17) into (2.12), the DC-link voltage dynamics is expressed by,

$$\frac{dV_{dc}}{dt}=-\frac{3v_d}{CV_{dc}}i_d+\underbrace{\frac{1}{C}\left((1-u_d)i_{PV}+(1-u_b)i_L\right)}_{Coupling\ term} \quad (2.18)$$

From (2.18), it can be observed that the DC-link voltage can be regulated through the current i_d. This regulation ensures the proper active power transfer through the inverter.

2.5 Water Cycle Algorithm for PI optimization:

To acquire the system stability, the accurate value of the controller parameter is essential. In the case of PI controller, trial and error is the most common tuning technique. Despite of the mathematical simplicity, the trail-error technique is inapt as it requires guessing and prediction. To deal with trail-error, the user needs to have some experiences in PI tuning prediction. To avoid this dissatisfactory trail-error approach, in this work WCA-based PI optimization has been used for DC-link voltage control and battery current control. Here, k_{p1} and k_{i1} are the corresponding

parameters for DC-link voltage regulator, while k_{p2} and k_{i2} are the battery current control parameters.

Water Cycle Algorithm (WCA) as an optimization method, underlies the fundamental concepts and ideas inspired by nature and based on the observation of water cycle process and how rivers and streams flow to the sea in the real world [81]. Water cycle optimization (WCO) is a technique, developed in [81], based on the water movement in nature. It consists of several phases such as evaporation, precipitation, and surface run-off [82], [83]. As we observe in nature, streams flow into rivers and rivers flow into the sea [82]. The searching process will conclude when the optimum solution is found, which is the sea position. The complete process is presented in the flow-chart in Figure 2.8.

The vector of raindrops position can be expressed by

$$\begin{cases} X=[x_1,\ x_2,\ x_3,\ x_4]=[K_{p1},K_{i1},K_{p2},K_{i2}] \\ \quad LB\leq x_i\leq UB; \quad i=1\cdots 4 \end{cases} \tag{2.19}$$

where, LB is the lower bound and UB is the upper bound.

Initially, the optimization algorithm generates a population of raindrops of the following positions

$$\begin{bmatrix} X^1 \\ X^2 \\ \vdots \\ X^N \end{bmatrix} = \begin{bmatrix} x_1^1 & \cdots & x_4^1 \\ \vdots & \ddots & \vdots \\ x_1^N & \cdots & x_4^N \end{bmatrix} \tag{2.20}$$

where, N is the size of the population, X^i is the raindrops position and $i = 1, \cdots, N$.

The position X^i, $i = 1, \cdots, N$, are randomly generated by

$$X^i=LB+(UB-LB)\times rand(1,N) \tag{2.21}$$

In the searching process, the objective is to tune control parameters in order to minimize the tracking errors $e_i = i_L^* - i_L$ and $e_v = V_{\mathrm{dc}}^* - V_{\mathrm{dc}}$. Therefore, the cost function, to be minimized, is selected such as

$$CF(X^i)=F(e_b,t)+F(e_v,t) \tag{2.22}$$

where, F is a function of the tracking error and the time.

The cost functions, $CF\left(X^i\right)$, $i = 1, \cdots, N$ are sorted in ascending order. The number, N_{sr}, of the best raindrops, with minimum CF values, are chosen to be $N_{\mathrm{r}} = N_{\mathrm{sr}} - 1$ number of rivers and the one with lowest cost function in the sea, where its position is the optimal solution.

The rest of the population, $N_{\mathrm{st}} = N - N_{\mathrm{sr}}$, includes the streams that can flow to the rivers or directly flow to the sea.

The streams are assigned to the rivers or the sea-based on the flow intensity of the raindrop provided by [2.21], [2.22]

$$NS_n = round\left\{\left|\frac{CF(X^n)}{\sum_{k=1}^{N_{sr}} CF(X^k)}\right| \times N_{st}\right\},\ n=1,2,\cdots,N_{sr} \tag{2.23}$$

where, NS_n is the number of streams that will flow into certain rivers and sea.

The streams, X_{str}, and the rivers, X_{riv}, will be changing their positions to move towards the rivers and the sea, X_{sea}, respectively. The new positions for the streams and the rivers are given by

$$\begin{cases} X_{str}(k+1) = X_{str}(k) + rand \times C \times (X_{riv}(k) - X_{str}(k)) \\ X_{riv}(k+1) = X_{riv}(k) + rand \times C \times (X_{sea}(k) - X_{riv}(k)) \end{cases} \tag{2.24}$$

where, k is the iteration number, $\mathrm{rand} \in [0 \quad 1]$ and C is a positive number.

The costs of the new positions (2.24) are carried out using the procedure (2.22). If the stream cost is found to be less than the river cost, their positions will be exchanged. The same procedure occurs for the river's positions and the sea position. The river position, with the lowest cost, becomes the sea position.

In order to prevent the rapid convergence of the optimization algorithm, the evaporation process occurs for the seawater in order to leave space for the rivers or streams to flow to the sea. This process is based on the following condition

$$if\ \left|X_{sea}^i - X_{riv}^i\right| < d_{max} \tag{2.25}$$

where, $i = 1, 2, \cdots, N_{\mathrm{sr}} - 1$ and $d_{\max}$ is a small number ($\rightarrow 0$).

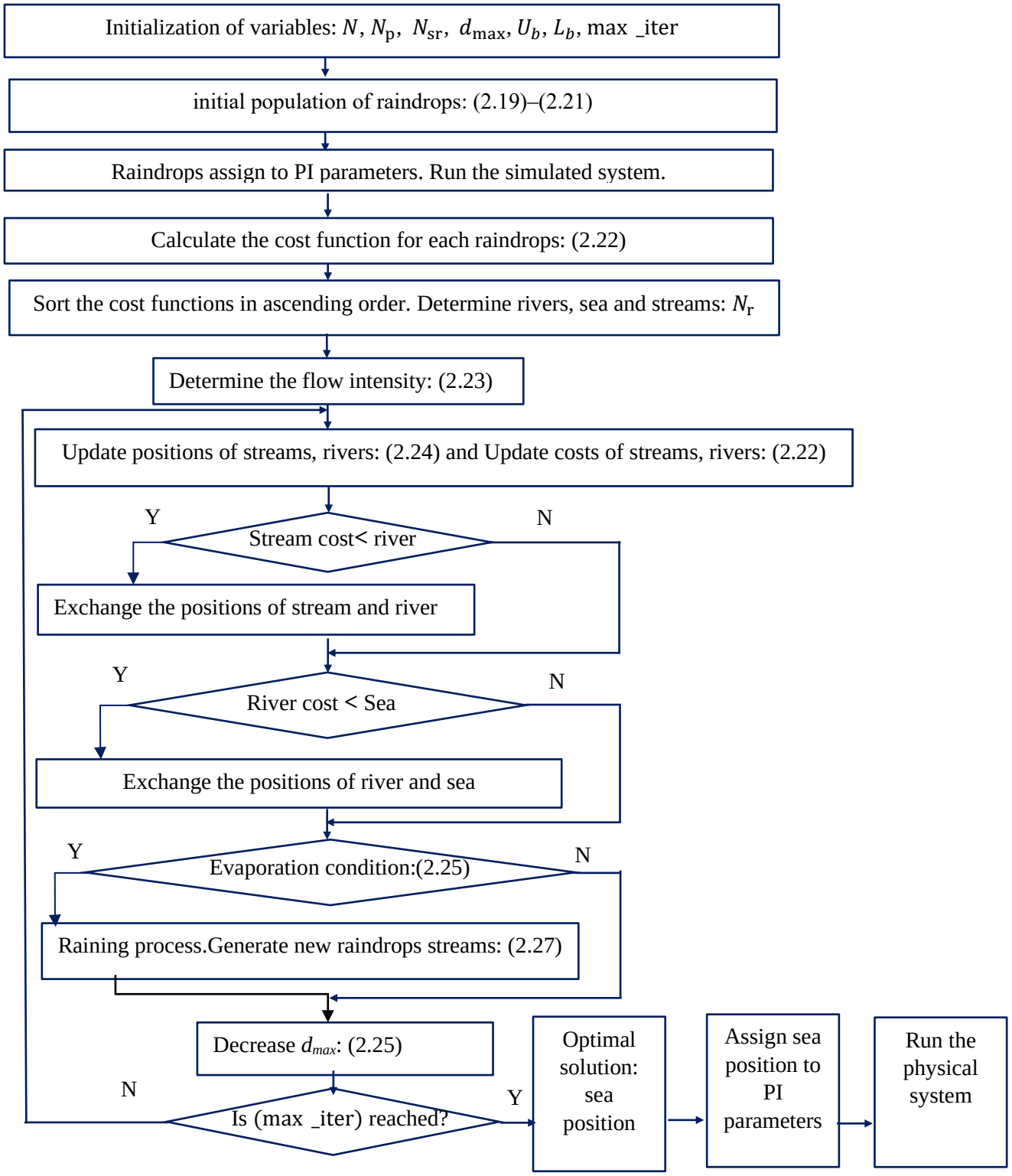

Figure 2.8: Process of PI optimization using WCA.

A distance, between the river and the sea, smaller than d_{max} indicates that the river has reached the sea. Therefore, the evaporation process can be applied and after enough evaporation, the raining process can start as observed in nature.

In order to reduce the search near the sea, the distance $d_{\max}$ is decreased as follows;

$$d_{max}(k+1)=d_{max}(k)-\frac{d_{max}(k)}{max\ \ \_iter} \tag{2.26}$$

Where, max _iter is the number of iterations and $k = 1, 2, \cdots, \max$ _iter.

The raining process occurs by creating new raindrops for streams in different positions such as

$$X_{str}^{new}=LB+(UB-LB)\times rand(1,N) \tag{2.27}$$

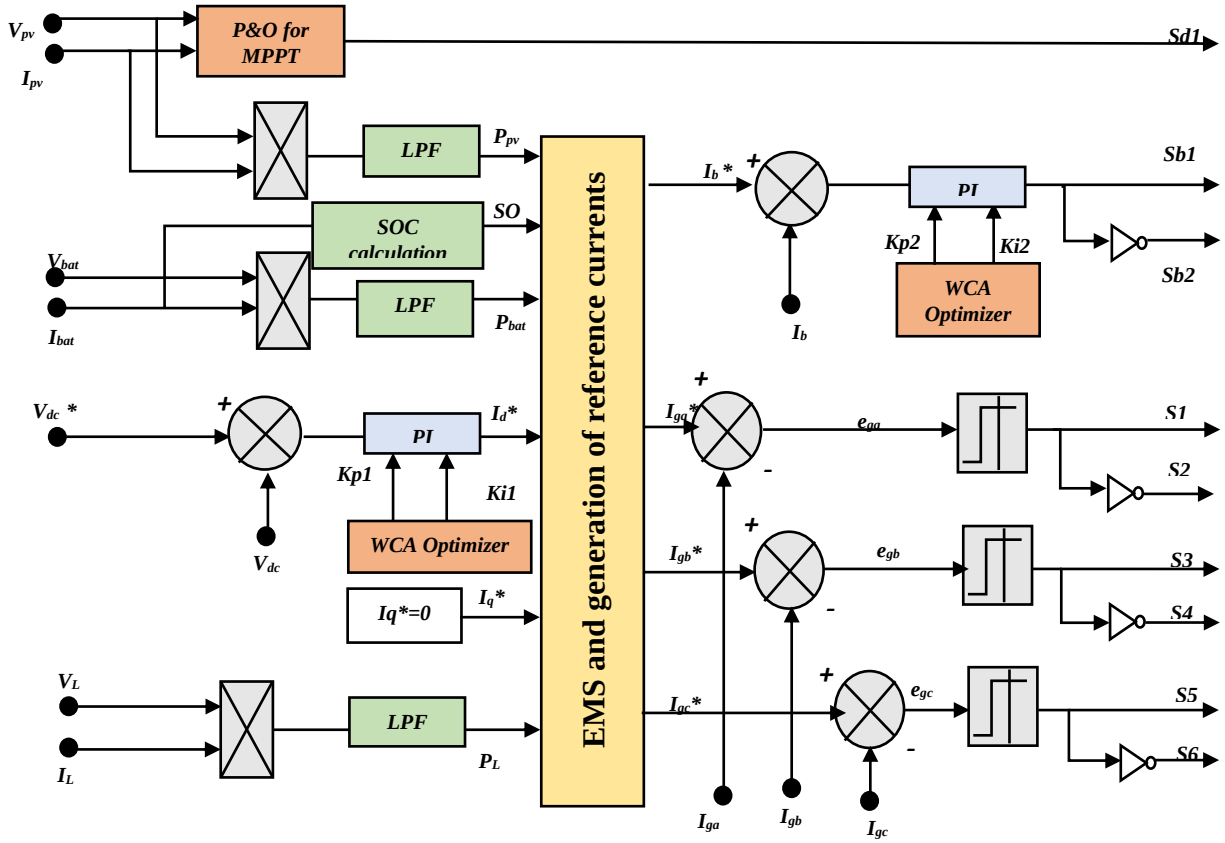

Figure 2.9: Overall controller configuration for the proposed microgrid.

Then, the next search proceeds from (2.20) until reaching the last iteration (max _iter). Finally, the sea position is the optimal solution, and its values will be assigned to the PI control parameters

(2.19). The cost function (2.22) is formulated in simulation and later on, the optimized value is used in the experimental microgrid.

The discussed controllers in prior sections are presented in Figure 2.9, which gives an overall idea about the control configuration. Besides, it gives a notion of interconnection among all local controllers, EMS generation, and WCA optimization.

2.6 Conclusion:

This chapter gives an overall idea of the proposed microgrid and its control units. The mathematical modeling has been elaborated with their schematic diagrams. The derived mathematical expression will be used in the implantation. The results and performance of the implemented microgrid will confirm the validation of the controller design.

Chapter 3: Energy Management System

3.1 Introduction:

Distributed energy resources are the small unit of power generation generally refers as a microgrid. The integration of DG and RES along with the battery storage is required for microgrid optimal operation [13], [21]. The prime focus of any microgrid establishment is the energy management system, as it works as the heart of the system. A functional microgrid unit without an efficient EMS is nothing but a waste of money and effort. While designing EMS there are constraints in different sections that need to be accounted. Since renewable resources such as solar irradiance, wind speed etc. are variable with any timespan, the prediction is inevitable for EMS design. Along with the DES, the load demand and the market price need to be predicted. Microgrid EMS can focus on different areas of interest like [11]-[20], economic benefit, clean energy, saving storage device, back-up generating units, supplying high load demand etc. Regardless the intension of microgrid establishment, the control approach needs to ensure the priorly.

In past years researchers have studied different microgrid and EMS techniques [60] - [72]. Some studies focus on the generating-side EMS, whereas some focus on the load-side EMS. Different research works have been carried out on the uncertainty and optimization of EMS. A bunch of simulations on EMS have been reported, while very a few EMS are operating in large-scale commercial microgrid. On the other hand, a satisfactory amount of laboratory-scale microgrid has been investigated over the past decades. In past reports, two modes of EMS operations have been discussed, namely centralized and decentralized. In the centralized mode aims to optimize the microgrid power exchanged based on the market prices and security constraints. On the other hand, decentralized mode deals with more degrees of freedom [63]. The crucial duty of EMS in both modes is to ensure power balance, and power trading in among generation, load, and grid.

In this chapter, firstly an overview of a different kind of microgrid EMS will be introduced. Then, some limitations and constraints of other EMS will be discussed. And finally, the EMS for the research project will be proposed and elaborated.

3.2 Survey on EMS Techniques:

There is no defined classification of microgrid system, as it can be differentiated based-on the perspective. In different literature different approaches have been applied to classifying microgrid and the EMS [55], [68]. In this report, the EMS has been classified in four types:

a) EMS for Traditional generators.

b) Energy storage-based EMS.

c) Load-side EMS.

d) EMS for a hybrid system.

For the traditional generator such as diesel turbine, steam turbine, hydro turbine, etc. EMS is designed with a storage system. The traditional plants can also be driven via simple or complicated EMS. In the second case, the energy storage system maintains the power balance between generation and consumption by storing power during inexpensive or off-peak hours and discharges when high-price or peak hours. Here, intelligent systems are used for prediction and EMS generation. Some common techniques for advance EMS are ANN, ANFIS, GA, WCA etc. In this category, algorithms generate the reference current for energy storage and maintain the power trades in every section of the network. For load-side EMS, energy consumption is reduced which improves efficiency [74]-[78]. Moreover, usage modification is considered in the EMS according to price and peak-hours. For the last category, a hybrid EMS is noticed which could be consisted of any two or three EMS discussed priorly to perform multi-objectives [77]-[83]. This kind of EMS can be implemented for large-scale generations or multi-purpose microgrid. It considers all the factors: hybrid generating units, market prices, load variations, predictions, faults etc. all together in the EMS.

3.2.1 Prediction Techniques in EMS:

The prediction of uncertain parameters can be performed over various time horizons ranging from short-term prediction to several years as a long-term prediction. Auto-regressive integrated moving average (ARIMA), generalized auto-regressive conditional heteroskedasticity (GARCH), dynamic

regression (DR) are some commonly used prediction techniques [35]-[40]. Some advanced techniques like, ANN, FLC can be implied in predictions. Some common uncertainty determinations methods are stochastic methods; point estimation method; scenario generation method; FLC and ANN; particle swarm, WCA, and GA algorithms. In Figure 3.1, the classification of prediction and uncertainty is depicted.

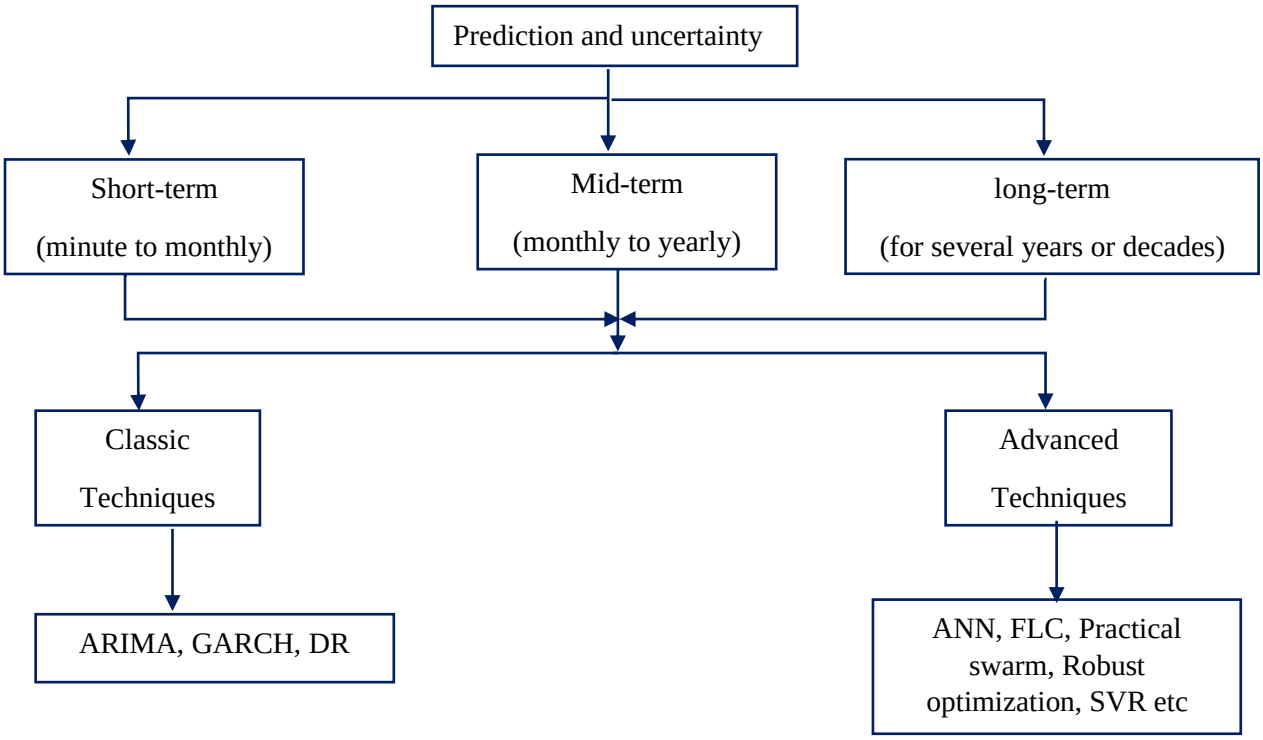

Figure 3.1 Classification chart of prediction and uncertainty in EMS.

3.2.2 Constraints in Existing models:

A power system without constraints is an unlikely phenomenon, hence constraints in microgrid EMS is the usual factors that draw great attention from researchers. Microgrid constraints include power limitations of generating units; power balance in generation and consumption; battery SOC limit and charge-discharge rate; battery life; switchgear limitations etc. [54]. Different research articles focus on different constraint [42], however considering all the constraints in a single EMS is quite impossible. Moreover, taking account of too many factors make the EMS complicated and infeasible for real-life usage.

Some literate discuses about the battery constraints, where other focuses on battery life [84]-[89]. In some agent-based microgrid, a lot of contains are considered, however they are only implemented in the simulation platform [57]-[60]. While working with source prediction author are ignoring battery life or market price for simplifications [63], [90]. In practical microgrids sometimes predictions methods are not considered. As a result, a lot of people have applied different optimization techniques to overcome these constraints and limitations.

3.3 Proposed EMS:

In this work, a PV and battery storage-based DC-microgrid and EMS have been designed. As it is already discussed that EMS can be designed in different ways for different applications. Algorithm-based intelligent EMS can compute complex scenarios, however, in most of the cases they are time-consuming [91], [92]. Even though, such intelligent EMS is still not feasible for a practical microgrid. Thus, in this research, a rule-based EMS has been proposed. A rule-base EMS refers to a condition-based outcome system, where the output follows the predefined rule provided by the user. The purpose of the EMS is to generate a current reference for the battery storage according to rules. A microgrid owner can not solely control generating units or load are as they are related to resources or consumers. In the contrary, the owner can control the charging and discharging of battery storage and can dominate the overall microgrid. As a result, for different rules the battery current will be changed in this proposed EMS. For generating the scenarios, the following inevitable constraints have been considered in the EMS:

(1) Battery state or SOC.

(2) Battery capacity.

(3) Grid availability.

(4) Dynamic price of the utility.

(5) PV and load variance.

(6) Optimal condition.

Taking consideration of these factors, eight operating modes have been prosed from the predefined rules. The operating modes are given as follows:

(i) Grid suit mode (GSM).

(ii) Battery suit mode (BSM).

(iii) Islanded mode (ISM).

(iv) Standstill battery mode (SBM).

(v) Cost effective mode (CEM).

(vi) Profit making mode (PMM).

(vii) Insufficient power mode (IPM).

(viii) Excess power mode (EPM).

In this research purpose, the dynamic billing of Nova Scotia, Canada is considered. The unitality price is taken from Nova Scotia Power official website [93]. The following symbols are explaining the appropriate terms:

Table 3.1: Billing rate of different hours of operation.

Symbol	**Referring term**	**rate/ kilowatt hour**
$\$$	Instantaneous utility price	Depends on the hour of operation, it can be any of $\$_{std}$, $\$_L$, $\$_H$
$\$_{std}$	Standard billing of utility	15.805¢/ kWh
$\$_L$	Off-peak hour rate	8.878¢/ kWh
$\$_H$	On-peak hour rate	20.163¢/ kWh

In this EMS it is considered that PV is always operating at MPPT and the power-grid is an ideal three-phase source. While the grid is contributing to supply load demand it is referred as grid-connected mode (GCM). In case of operation in GCM, the required grid power, to meet the load demand is carried out by

$$P_g = P_L - (P_{PV} + P_{bat}) - P_{loss} \tag{3.1}$$

where, P_L is the load demand, P_{loss} represents the power losses in the RL filter, due to the efficiency of the converters and other devices in the network.

The dynamic power flow between the battery and the power-grid is determined by an optimization factor, β. β will be a multiplication term with the reference battery current which will control the contribution of battery current toward the load. Since gird current contributes according to the battery current contribution the β factor indirectly controls the grid-supply current as well. The value of β factor is estimated using FLC for this EMS application. Figure 3.2 presents the FLC-

based β estimation where $ is the input and β is the output. The $ input is three triangular inputs: low; average and high. Similarly, triangular outputs for low, average, and high values of β are taken into account. The input-output relation of $ and β is also provided in the same figure. The scaling of the billing for input is considered from Nova Scotia Power website which is given in Table 3.1. The output β, is always less than 1. So, it can be deduced that with the increment of $ the value of β increases, which refers the current from the battery will increase. In contrast of that, the power consumption from the utility grid will be decreased. In this EMS, another factor is considered for compensating the losses that occurred in different sections of the microgrid. Here, the loss compensation factor, α (α<1), increases the battery current to compensate for the loss by the battery current. To determine the value of α trail-error based approach was carried out. Every time the power balance in the load side and generating side was matched by tunning the value of α.

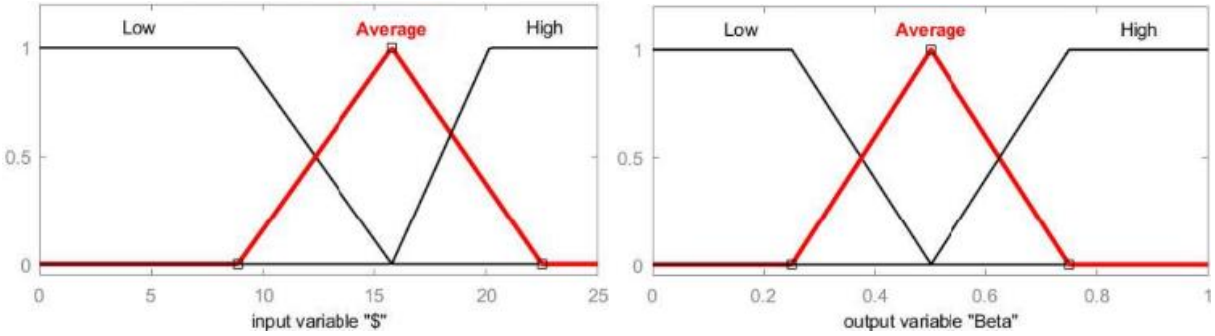

(a) (b)

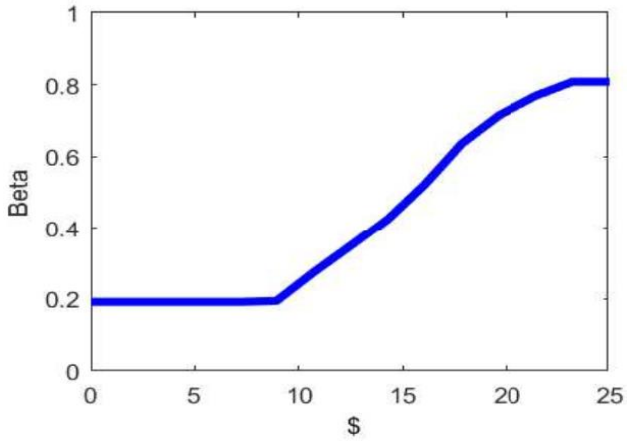

(c)

Figure 3.2 Membership functions: (a) Input ("$"); (b) Output (β) (c) input-output relation

The proposed rule-based EMS is depicted in a flow-chart in Figure 3.3. The elaboration of each mode is given in succeeding sections.

(i) GSM:

For the very first mode, the conditions assumed are: battery SOC is within limit; PV power is close to zero or minimum and load is fixed. The network is grid-connected; however, the utility price is less than standard price. For this instant, the grid needs to supply most of the load demand to make the microgrid economical. Here, by considering $\beta < 0.5$, the battery discharge has limited, while grid contribution is increased. In addition, α is compensating the system losses by providing current from the battery storage. For GSM, the battery current reference is expressed by

$$\begin{cases} I_{bat}^{*} = \frac{\beta \cdot P_L}{\alpha \cdot V_{bat}}, & \{P_{PV} \approx 0;\ \$ < \$_{std}\} \\ \beta < 0.5 \end{cases} \tag{3.2}$$

(ii) BSM:

For the BSM mode, the assumed conditions are identical as GSM except for the utility price. Here, the utility price is higher than the standard price. So that, the battery needs to supply most of the load demand to avoid grid contribution and save money. Here, by considering $\beta > 0.5$, the battery discharge has increased, while grid contribution is limited.

The battery current reference for BSM is given by

$$\begin{cases} I_{bat}^{*} = \frac{\beta \cdot P_L}{\alpha \cdot V_{bat}}, & \{P_{PV} \approx 0;\ \$ > \$_{std}\} \\ \beta > 0.5 \end{cases} \tag{3.3}$$

(iii) ISM:

ISM refers to islanded mode condition which clearly indicates zero power consumption from the grid. From now on, it is considered that PV has returned as sunny conditions and PV provides maximum power. In this condition, the load will be supplied from the PV and battery, as the grid is unavailable. This condition is valid if enough battery power is available to meet the demand, otherwise, the load shedding is required for power balance. For clarification, it is to be mentioned that ISM is the only condition where the grid is isolated. In other seven conditions of the EMS are grid-connected. ISM battery current reference can be expressed as.

$$I_{bat}^{*}=\frac{P_L-P_{PV}}{\alpha \cdot V_{bat}}, \qquad \begin{Bmatrix} P_g \approx 0;\ P_L=P_{PV}+P_{bat}; \\ SOC_{min} \leq SOC \leq SOC_{max} \end{Bmatrix} \tag{3.4}$$

(iv) SBM:

Deep-charging and deep-discharging are common scenarios in battery storage. Deep charging occurs while other than battery there is other generators to supply the load demand. So, battery discharge at a high rate and SOC exceeds it SOC_{min} limit. The reverse scenario happens when there is an excess of power in the microgrid and the battery charge state crosses it SOC_{max} limit. In general, any EMS is required to take into consideration the battery constraints related to the SOC for safety. In such a condition for the proposed EMS, the battery becomes standstill or idle, and provides no power means zero current to the network. For the EMS, SBM is the only condition where the battery becomes standstill. So, the battery current reference for SBM is;

$$I_{bat}^{*}=0, \qquad \{SOC<SOC_{min}\} \tag{3.5}$$

(v) CEM:

If the grid price is at the off-peak rate, then the EMS switches to Cost-effective mode. In this condition grid, PV and battery power is available. Since the grid has power at a low rate, the intension is to supply the load and charge to battery at the maximum rate from the grid. The battery current reference is given by

$$I_{bat}^{*}=-I_{bat\_max}, \qquad \{\$ \approx \$_L;\ SOC \leq SOC_{max}\} \tag{3.6}$$

(vi) PMM:

It's a grid-connected condition, where the grid price is high at on-peak rate and the load demand will be met by the PV and battery. In addition, the available energy from the microgrid can be sold to the grid for profit. This scenario normally occurs during on-peak hours to take advantage of the high price ($\$_H$). In this mode, the battery can be discharged at maximum rated current (I_{bat_max}) until reaching the limit (SOC_{min}) if required. The battery current reference is given by

$$I_{bat}^{*}=I_{bat\_max}, \qquad \{\$ \approx \$_H;\ SOC_{min} \leq SOC\} \tag{3.7}$$

(vii) IPM:

This mode refers to the condition when the load demand is higher than the generated power. For the IPM mode condition assumed are: standard utility price, high load, PV and battery power available and grid is connected. In this case, the battery discharge is optimized based on the grid

price by assigning the optimization factor (β) a value proportional to the grid price. The battery current reference is expressed by.

$$\begin{cases} I_{bat}^{*}=\frac{P_L-\beta\cdot P_{PV}}{\alpha\cdot V_{bat}}, & \{\$_L<\$<\$_H\} \\ & \beta\propto\$ \end{cases} \tag{3.8}$$

(viii) EPM:

In case of surplus power from the PV source than the load demand, and the grid price is between the low and high rates, the battery can be charged at an optimum rate and selling the remaining power to the grid. For both IPM and EPM, the rate of charging and discharging of the battery, as well as grid contribution, depends on the factor β. The battery current reference for EPM is expressed by

$$\begin{cases} I_{bat}^{*}=\frac{P_L-\beta\cdot P_{PV}}{\alpha\cdot V_{bat}}, & \{P_L>P_{PV};\ \$_L<\$<\$_H\} \\ & \beta\propto\$ \end{cases} \tag{3.9}$$

The eight modes of operation can be summarized with the constraints in Table 3.2.

Table 3.2: EMS operating modes summarization.

Mode	Conditions	Reference current
GSM	$P_{PV}\approx 0;\ \$<\$_{std}; \beta<0.5$	$I_{bat}^{*}=\frac{\beta\cdot P_L}{\alpha\cdot V_{bat}}$
BSM	$P_{PV}\approx 0;\ \$>\$_{std};\ \beta>0.5$	$I_{bat}^{*}=\frac{\beta\cdot P_L}{\alpha\cdot V_{bat}}$
ISM	$P_g\approx 0;\ P_L=P_{PV}+P_{bat};$ $SOC_{min}\leq SOC\leq SOC_{max}$	$I_{bat}^{*}=\frac{P_L-P_{PV}}{\alpha\cdot V_{bat}}$
SBM	$SOC<SOC_{min}$	$I_{bat}^{*}=0$
CEM	$\$\approx\$_L;$ $SOC\leq SOC_{max}$	$I_{bat}^{*}=-I_{bat\_max}$
PMM	$\$\approx\$_H;$ $SOC_{min}\leq SOC$	$I_{bat}^{*}=I_{bat\_max}$
IPM	$\$_L<\$<\$_H;\ \beta\propto\ \$$	$I_{bat}^{*}=\frac{P_L-\beta\cdot P_{PV}}{\alpha\cdot V_{bat}}$
EPM	$P_L>P_{PV};\ \$_L<\$<\$_H;\ \beta\propto\ \$$	$I_{bat}^{*}=\frac{P_L-\beta\cdot P_{PV}}{\alpha\cdot V_{bat}}$

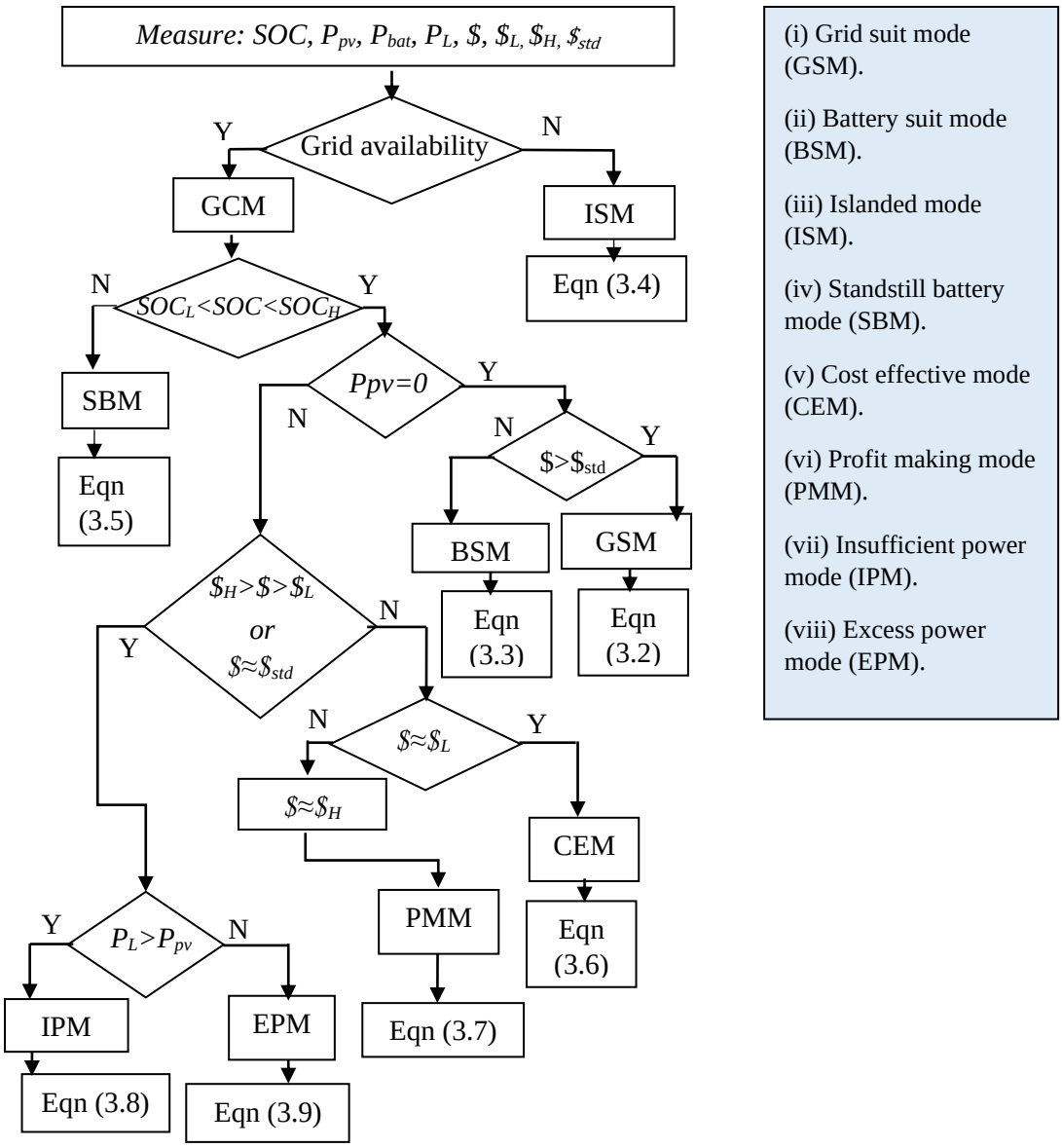

Figure 3.3: Flow-chart of the prosed microgrid EMS.

3.4 Conclusion:

In a nutshell, this chapter is a detailed discussion of the proposed EMS. All the operating modes have been elaborated with the applied condition. In the next chapters, this EMS will be implemented for the designed microgrid. The responses from the implementation will verify the performance of the EMS.

Chapter 4: Digital Real-Time Simulation Environment

4.1 Introduction:

Digital real-time simulation (DRTS) can reproduce a real system wheatear it's a power system or power electronic network. This DRTS mimics a real system and generates the required control signals. For this purpose, a digital real-time simulator has to solve the model equations for one time-step within the same time in real-world clock [94]-[98]. In such DRTS system, a dedicated software uses its tools to replicate the physical system and by solving the computation in FPGA it generates the control pulses.

In power system application mostly two types of DRTS is used:

1) fully digital real-time simulation

2) hardware-in-the-loop (HIL) real-time simulation.

In full DRTS, action such as, control, protection, and other accessories, are modeled inside the simulator and does not involve external interfacing or inputs/outputs (I/Os). On the other hand, the HIL simulation refers to the condition where parts of the fully digital real-time simulation have been replaced with actual physical components [96]-[98].

In this chapter, firstly the brief description of DRTS will be presented with a communication protocol. Then, the experimental test-bed will be introduced with proper descriptions. Finally, the acquired results from the experiment will be evaluated.

4.2. Description Of Digital Real-Time Simulation:

Among the available simulators OPAL-RT is technically more viable for its fast-reliable operation and performance. OPAL-RT simulator accommodates eMEGAsim, HYPERSIM, eFPGAsim, ePHASORsim which are hardware integrated software [97]. It notable that, eMEGAsim is a more flexible and scalable DRTS which includes RT-LAB, ARTEMIS, and RTE Event software.

In this research work, a HIL-based DRTS has been used for the modeling and control. OPAL-RT interfaces: OP5600 and OP8600, are respectively used for data acquisition and real-time

simulation with the help of RT-Lab software. The detail explanations are given in succeeding sections.

4.2.1. OP5600 and OP8600 interfaces:

The high-performance simulation hardware, OP5600 real-time simulator is the most adopted simulation platform by OPAL-RT's users in industry and academia. OP5600 combines the performance, versatility and reliability that is ideal for demanding hardware-in-the-loop applications. Whether working within the power systems, aerospace, automotive, oil and gas or other electro-mechanical industries, the OP5600 has the power to simulate systems, while offering all the I/Os required to get your hardware into the loop [98]. The OP5600simulator consists of an upper section that contains analog and digital I/O signal modules and a bottom section which contains the multi-core processor computer and FPGA that runs RT-LAB or HYPERSIM real-time simulation software platform. The OP5600 can be used either as a desktop system or rack-mounted as part of a network of OPAL-RT simulators communicating through high-speed PCI-e links. The chassis views are given in Figure 4.1.

(a) (b)

Figure 4.1: Chassis view of (a) OP5600 (b) OP8660.

The OP8660 is a HIL Controller and data acquisition interface designed to be used with the complete OP5600 simulation system to provide a supplementary signal conditioning. Its core contains four (4) OP5511 high current and high voltage input conditioning modules, which allow conversion of current and voltage to ±10V voltage signals. It is designed to be used either as a desktop (or shelf top) or as a more traditional rack mount. and uses standard connectors (DB37, DB9 and banana jack) without the need for input/output adaptors and allows quick connections for monitoring. The rear of the chassis provides the DB37 connectors that link the OP8660 to the OP5600 simulator, while the front provides connectors (banana jack or DB9) for connecting client-

side applications such as inverters, encoders, monitoring and measuring devices [83, [88]. By installing the HIL Controller as a link between the unit under test (ECU, motor controller, etc.) and the simulator, you can insert a fault at any point in the test to assess how the unit reacts to the fault.

4.2.2. Overview of RT-Lab and MATLAB/Simulink:

Opal-RT interfaces are associated with RT-Lab software. And, the RT-LAB software is based on SimPowerSystems of MATLAB/SIMULINK, which has the feature of modernizing model-based design in electric power systems. The main feature of this software is to meet the transient simulation requirements of electromechanical drives and electric systems. Wide accessibility, greater ease of use and more compatibility with commercial products are the vital leverages of this simulator. Additionally, Real-time software-in-the-loop (SIL) and Hardware-in-the-Loop (HIL) applications are gradually accepted as important tools for engineering design mainly in the power system field [96]-[99]. All these features are offered by this simulator are more intriguing for both academic and industrial applications. These features will improve the accuracy of the prediction of current and future needs of power.

RT-Lab enables MATLAB/Simulink models to interact with the real world in real-time. The primary use is to implement real-time, hardware-in-the-loop engineering simulators and rapid prototyping controllers. RT-Labworks by linking code generated with the Simulink Coder to highly-optimized runtime libraries. These libraries enable to leverage the full power of modern PC architectures, achieving jitter-free fixed-step sizes down to a few tens of microseconds. RT-Lab can run models quickly on SMP or distributed targets by automating the preparation, downloading, and running of parallel models. The RT-Lab family of products also includes specialized block-sets that help improve the precision and speed of real-time simulation.

RT-Lab can be used as engineering simulators and rapid prototyping controllers to prototype working controllers. Test engineers use RT-LAB to validate controllers against real-time, hardware-in-the-loop, dynamic MATLAB/Simulink models of the plant, be it a virtual vehicle, an aircraft or a missile, a robot, or an electric power system. RT-LAB also supports State flow and the Simscape Electrical.

4.2.3. Communication Protocol Of RT-Lab and OPAL-RT Interfaces:

The process of execution in RT-Lab and OPAL-RT is shown in Figure 4.2. As RT-lab works simultaneously with OPAL-RT interfaces, the communications in both systems is bidirectional. The overall communication protocol is shown in Figure 4.3. Firstly, OP8660 senses the physical electrical signals, voltage, and current, and process the data through OP5660, and send it to MATLAB/Simulink for controller design. And conversely, in real-time controller generated the requires pulses and send the signal to physical inverters and converters through OPAL-RT interfaces.

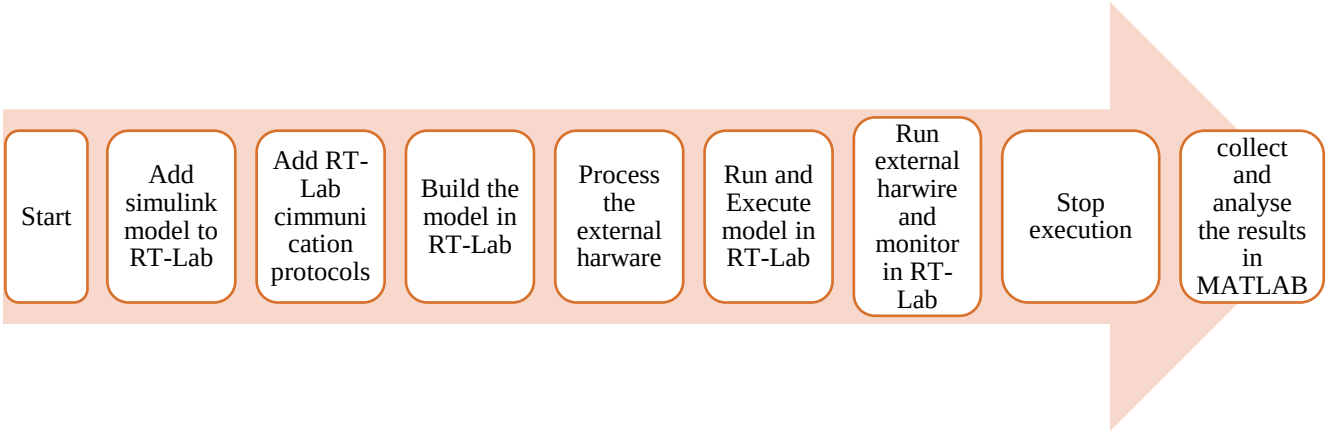

Figure 4.1: Process of RT-Lab complete execution.

The block diagram of the Simulink model must be modified by regrouping the model into subsystems and inserting OpComm blocks [88]. In RT-Lab, all the subsystems must be named with two prefixes based upon their function. The prefixes are console subsystem (SC_) and master subsystem (SM_). There is at least one OpComm block in the console subsystem (SC_). It contains all user interface blocks including scopes, displays, switches that run asynchronously from the other subsystems. Each master subsystem in RT-Lab is represented by a core that performs its processes in an efficient and fast way. In the RT-Lab model, there must be at least one master subsystem in each model. The master subsystem (SM_) contains all the computational elements of the model, the mathematical operations, the input and output blocks, and the signal generators. After grouping the model, OpComm blocks must be added to enable and save communication setup data. All inputs of subsystems must first go to OpComm block before being used. After connecting input/output hardware, the Simulink model is compiled in RT-Lab. Then, it is loaded in OP5600 real-time simulator for the master subsystem. Finally, all the subsystems are executed

by OP5600 simulator. In Appendix B. more information and elaboration for RT-Lab execution is given for better understanding.

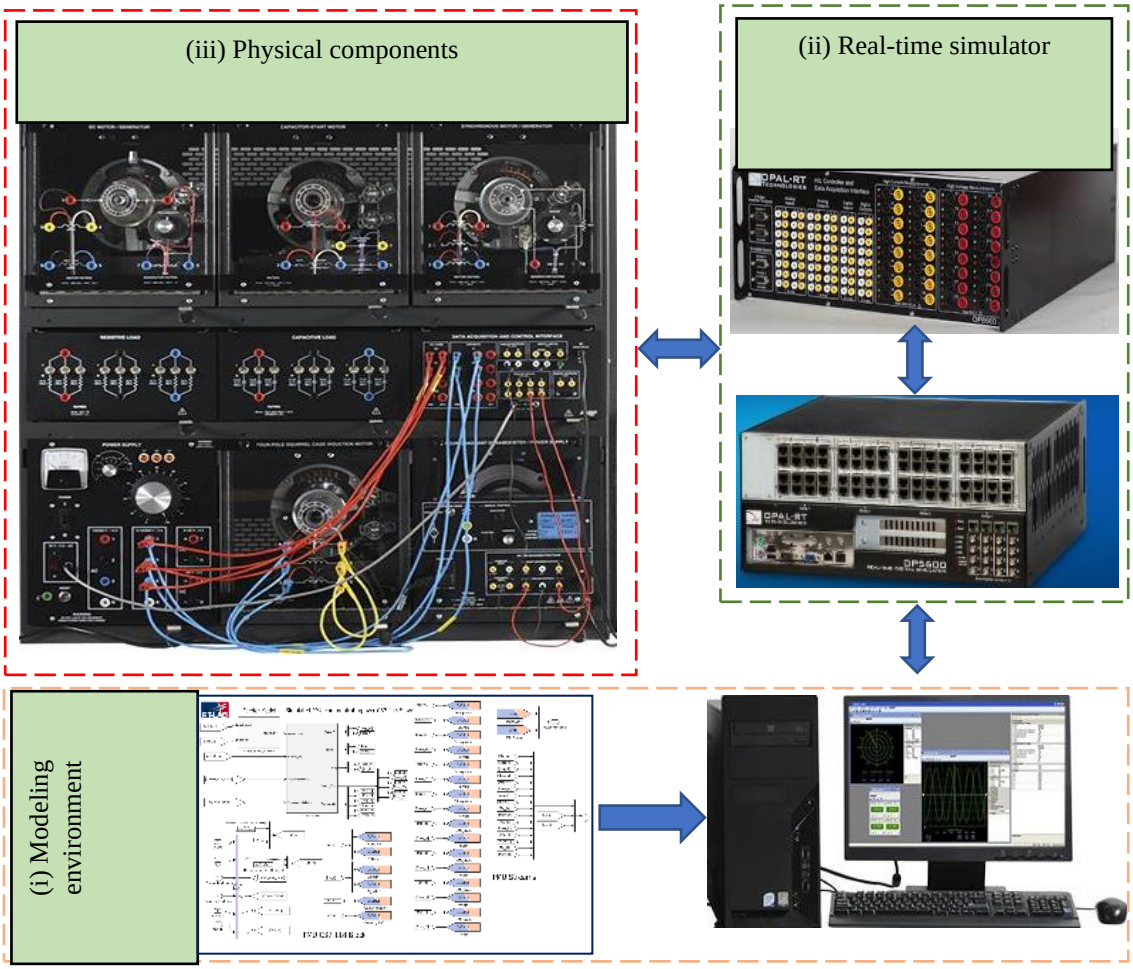

Figure 4.2: Communication protocol of the interfaces.

4.3. Conclusion:

In this chapter, the process of DRTS has been discussed. Firstly, brief discussion of the OPAL-RT interfaces is presented. Then, the interconnection between RT-Lab and Simulink modeling is discussed. Lastly, the complete communication prototyping is mentioned l this chapter.

Chapter 5: Experimentation and results

5.1. Experimental Setup:

In this work, a laboratory-scale PV and battery storage-based grid-connected microgrid is implemented using Festo LabVolt machines and power electronics as a physical system, whereas OPAL-RT interfaces were used for digital real-time simulation and data acquisition. PPPE is a distinct feature of *Magna power SL series programmable DC power supply which* is used as PV source in this work. In PPPE different profiles such as, high and low irradiance profile, different MPP point, different PV cells, can be selected. Moreover, I user can switch the profiles manually and automatically during the execution. Figure 5.1 shows the PV profile used in this microgrid research. For the energy storage system, a 48V, 9Ah LabVolt lead-acid battery is used for the practical testbed. The PV and battery are connected to a boost and buck-boost converter respectively, and the outer terminals of the converters are connected to the input of three-phase inverter. The inverter is a grid-connected voltage source inverter. To ensure the harmonic reduction and smooth output, filters are connected with converter and inverter circuits [100]. A three-phase variable balanced load is connected with the supply line to demonstrate the EMS and power balance in the network. For the filter and inverter, LabVolt inductor and IGBT modules are used. The complete connection diagram is depicted in Figure 5.2.

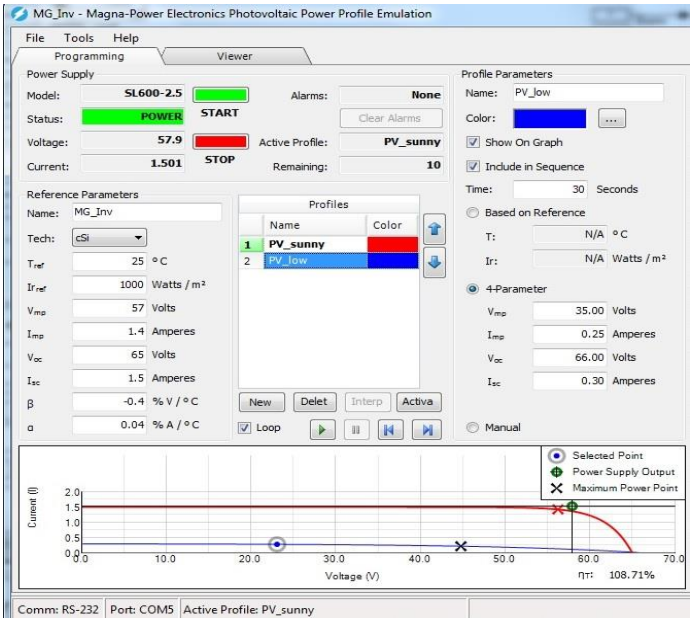

Figure 5.1: PV profile during experiment

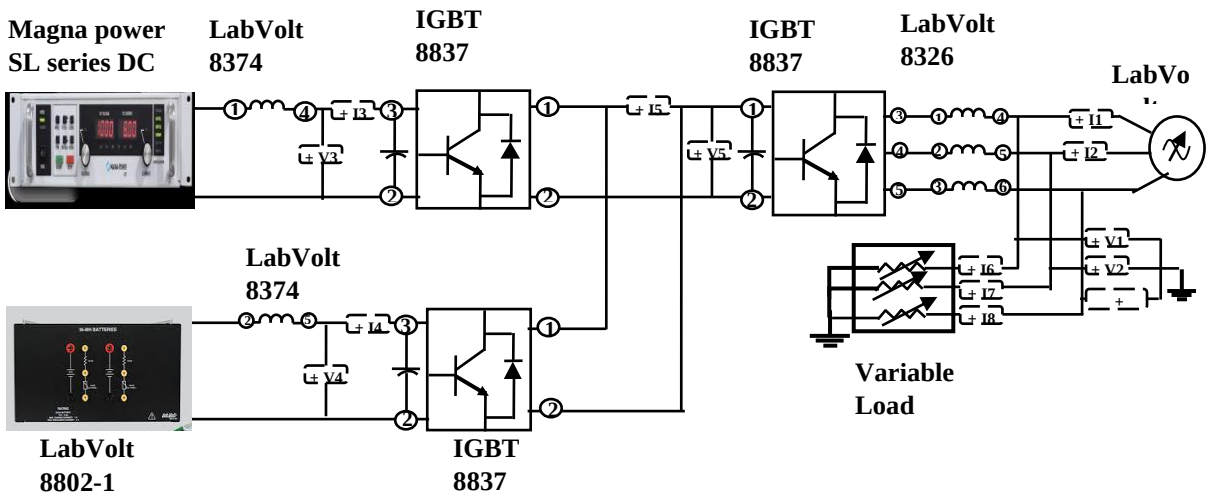

Figure 5.2: Connection diagram of PV and battery storage-based grid-connected microgrid.

According to the connection diagram, the microgrid has been implemented and tested in the Laboratory of Control Systems and Mechatronics, Saint Mary's University, Halifax, Nova Scotia, Canada. Figure 5.3 presents the physical experiment carried out for the validation of the proposed controller and EMS. The rating and components detail are given in Table 5.1.

Table 5.1: List of components.

Vendor Name	Product name (Rating)	Product ID
LabVolt Series by Festo Didactic	Line inductor (14mH, 5A, 400V)	Model 8374-A0
	IGBT Chopper/Inverter (420V, 6A)	Model 8837-BO
	Variable power supply (120/208V, 15A)	Model 8525-20
	Three phase filter (25mH, 5A, 400V)	Model 8326
	Lead-acid battery (48V, 9Ah)	Model 8802-1
Mathworks	MATLAB/Simulink	Matlab 11.b
Magna-Power	Programmable DC power supply (600V, 2.5A)	SL-600, 1.5kW
Opal-RT Technologies	Real time simulator	OPAL-RT OP5600
	HIL Simulator controller and Data acquisition Interface	OPAL-RT OP8660

The electrical signals from LabVolat and PV units are sensed and processed by OPAL-RT interfaces, while RT-Lab directs the processed signal to Simulink controllers. In real-time Simulink generates the control signals for the LabVolt IGBTs and sends back the discrete signals through RT-lab to OPAL-RT interfaces. The FPGA in OP5600 and OP8600 generate and provide the physical control pulses to IGBTs.

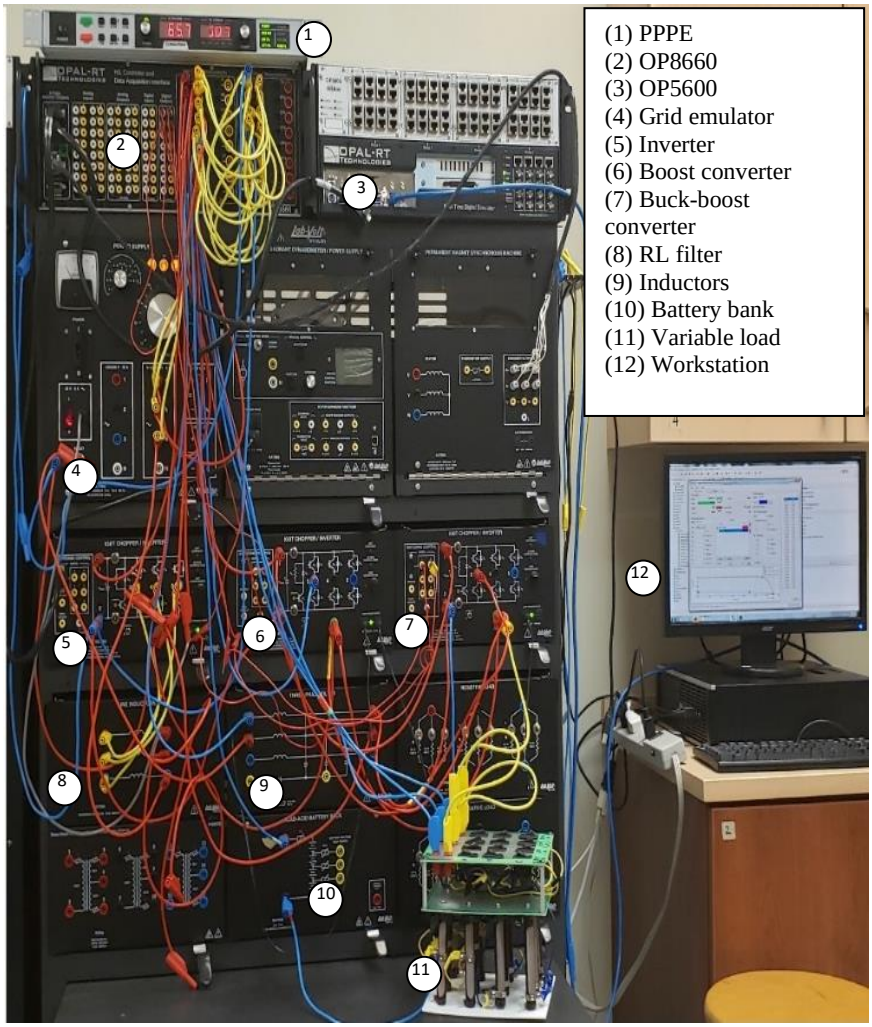

Figure 5.3: Experimental testbed for the microgrid.

5.2. Experimental Results:

5.2.1. Performance analysis of WCA:

In chapter 2, it is already discussed that WCA has been used instead of trail-error for PI optimization. An identical simulation platform is built and simulated as Figure 5.2 in Matlab/Simulink for the optimization. WCA can be determined for four types of performance indices: IAE, ISE, ITSE and ITAE. All these indices of WCA were running in offline mode in MATLAB/Simulink. And, from the results following Table 3.2 has developed. By analyzing and comparing the table is it clear that ITSE gives the best result. For the implementation of DC-link voltage controller selected PI parameters K_{p1}, K_{i1} are 0.7903, 0.9987, respectively. And for the battery current controller selected PI parameters K_{p2}, K_{i2} are 1, 0.9257, respectively. The fitness curve of ITSE for 100 iterations is depicted in Figure 5.4.

Table 5.2: Observation of WCA optimization

Index	**Parameters**	**Values**
Integral absolute error (IAE)	K_{p1}, K_{i1} K_{p2}, K_{i2} Best Elapsed time (sec)	0.7114, 1 1, 0.6205 1.4684 11588.400879
Integral square error (ISE)	K_{p1}, K_{i1} K_{p2}, K_{i2} Best Elapsed time (sec)	0.7892, 0.9997 1, 0.9494 1.0223 11317.054638
Integral time square error (ITSE)	K_{p1}, K_{i1} K_{p2}, K_{i2} Best Elapsed time (sec)	**0.7903, 0.9987** **1, 0.9257** 0.1046 11745.794817
Integral of time-weighted absolute error (ITAE)	K_{p1}, K_{i1} K_{p2}, K_{i2} Best Elapsed time (sec)	0.7839, 0.9998 1, 1 0.1430 11780.038236

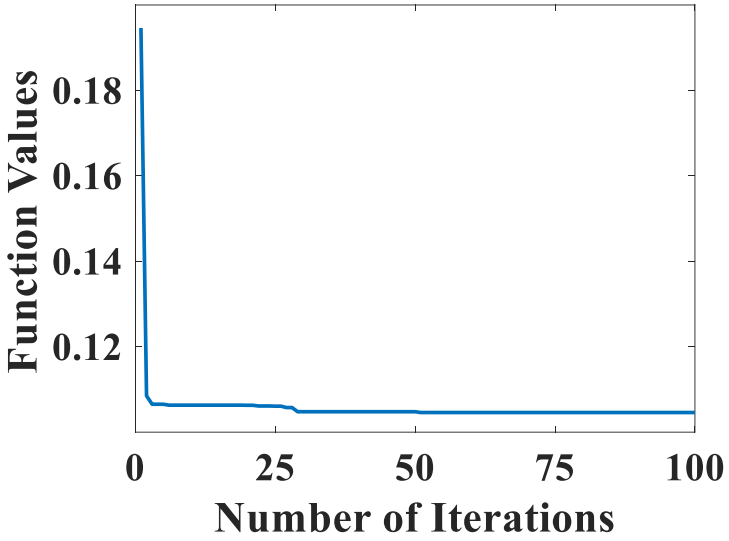

Figure 5.4: Fitness curve of ITSE.

The PI optimized value achieved from WCA-ITSE has been tested for two scenarios. The Simulink model is developed the same as Figure 5.2 and tested by changing several input references to observe the tracking performance of PI controller.

For the first scenario, conditions are:

1) PV irradiance is fixed at 1000 w/m^2, 2) fixed load at 138W,

3) Fixed DC-link voltage at 110V, 4) battery current fixed at 1A.

Figure 5.5 shows the DC-link voltage and battery current track. As references are kept constant the tracking is easy in this case. The results show that a perfect tracking in both controllers are achieved using WCA.

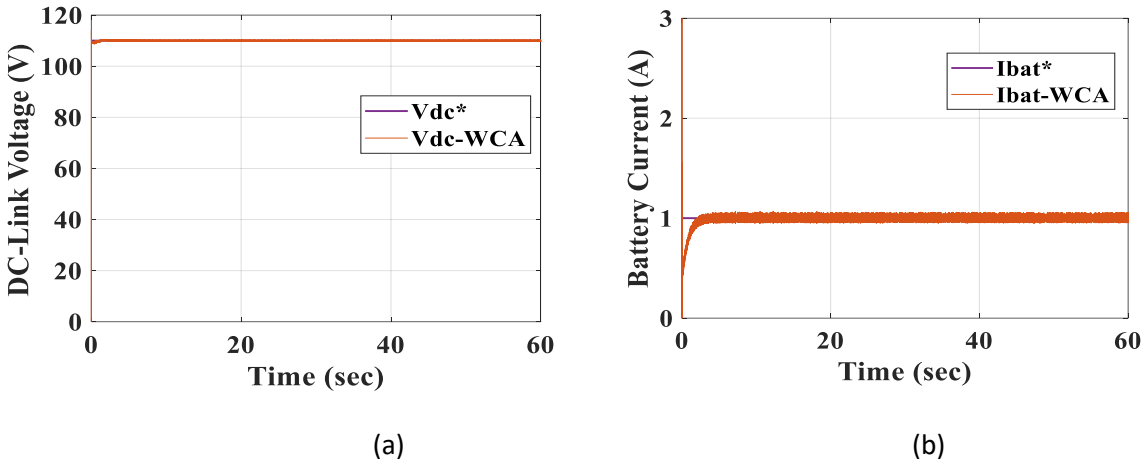

Figure 5.5: (a) Tracking of DC-link voltage reference, (b) Tracking of battery current reference.

For the second scenario, conditions are:

1) Variable PV irradiance is given in Figure 5.6, 2) Fixed load at 138W,

3) Step change of DC-link voltage, 4) step change of battery current reference.

In the 60 seconds of execution, the PV irradiance is changed randomly. The DC-link reference is stepped from 110V to 115V and again stepped down to 110V. Despite of the changes in DC-link voltage reference and irradiance the DC-link voltage is accurately regulated. However, small overshoots are generated while irradiance jumped dramatically, and battery current changed. Figure 5.7 shows the DC-link voltage and battery current tracking. For the battery current controller, precise control is achieved, although sharp overshoot happened at the current reference change point.

From these tests, it is confirmed that WCA has provided the optimized values for the controllers, which are quite acceptable for the further testing purpose.

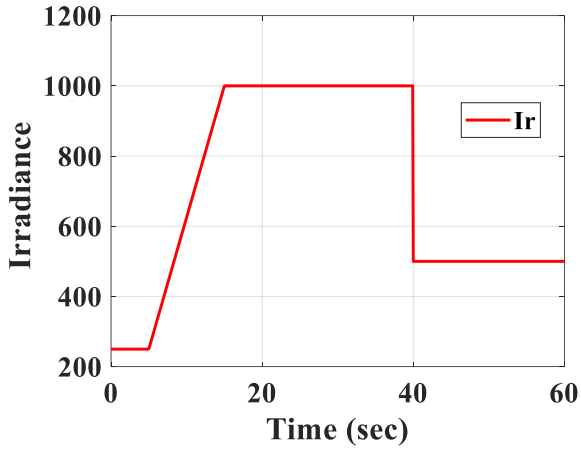

Figure 5.6: Variable irradiance profile.

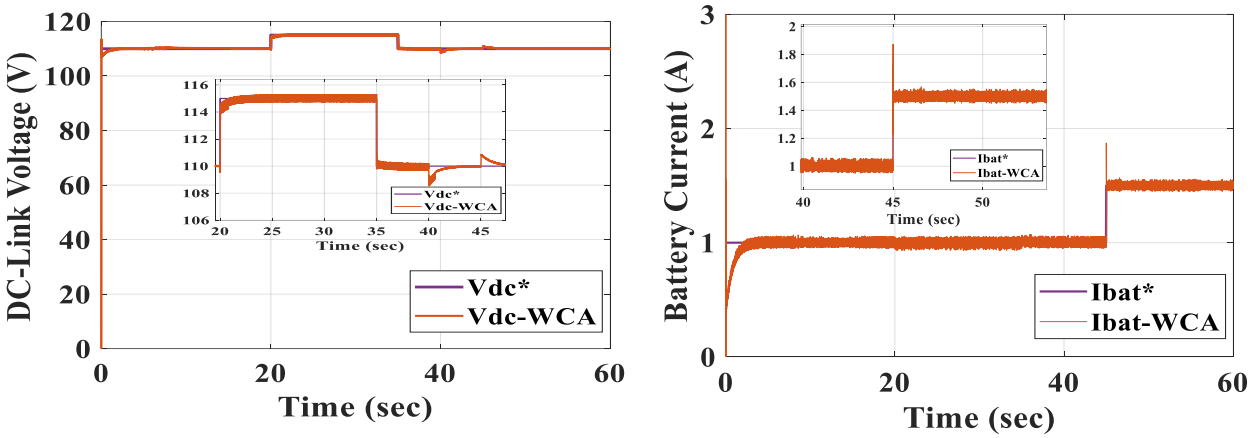

(a) (b)

Figure 5.7: (a) Tracking of DC-link voltage reference, (b) Tracking of battery current reference.

5.2.2. EMS test 1:

Among the eight operating modes proposed in the EMS in chapter 4, four modes are executed in a single test. Execution of eight scenarios in a single run-time would be confusing for understanding. The OPAL-RT-based LabVolt microgrid test-bed will be running for t=60 sec for each test. In order to demonstrate the four operating modes, modes are switched after each 15 sec intervals. After the execution MATLAB provides the experimental results since MATLAB workspace and scopes are used as data indicators in RT-Lab technology.

From t=0 sec to t=30sec, GSM is in operation while PV is low irradiance as given in Figure 5.1. As the price is lower than the standard price, the grid supplies a higher share of the 138W load

demand, and the battery provides less power according to equation (3.2). Figure 5.8 depicts the power response for the four modes of test 1. At t=15 sec, EMS switches to BSM, as grid price is higher than the standard price. Now in BSM, the battery supplies more power than the prior mode. In this condition, other conditions have remained same. At t=30 sec, PV irradiance is switched to sunny irradiance profile and PV starts supplying maximum power of 90W. Meanwhile, EMS switches to ISM mode which refers to zero power consumption from the grid-side. Therefore, PV and battery take care of the load demand. In the last mode SBM activated at t=45 sec, while battery exceeds its SOC_{min} limit and becomes idle and provides zero power to the network. In SBM, grid and PV supply the load demand.

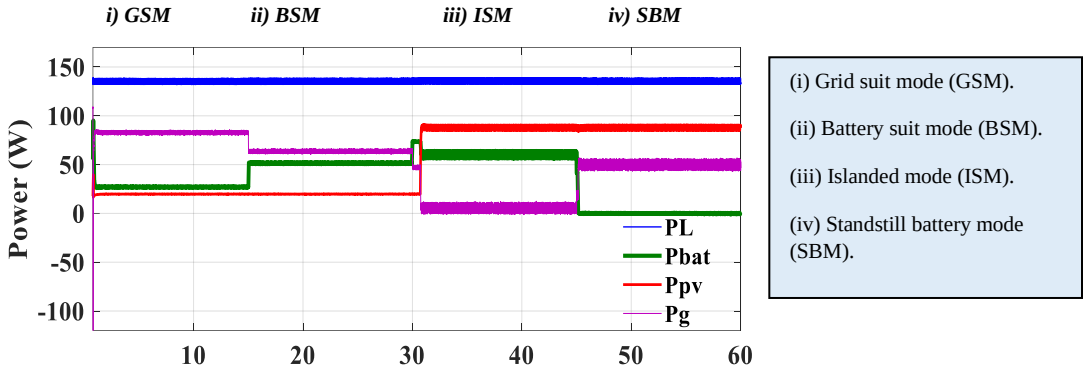

Figure 5.8: Power response in the microgrid system.

In Figure 5.9, PV and battery current have been presented. Until t=30sec, PV current is very low which increased to 1.5A after t=30 sec according to the irradiance profile. The battery current resembles the battery power and it precisely follows the battery reference generated from EMS. As we know, while battery discharge increases the SOC value decreases which is presented in Figure 5.10. Initially SOC was 60%, which descending to 59.9%, 59.75% and 59.5% at GSM, BSM and ISM respectively. Moreover, SOC becomes standstill while battery stopped supplying power at SBM for exceeding SOC limit.

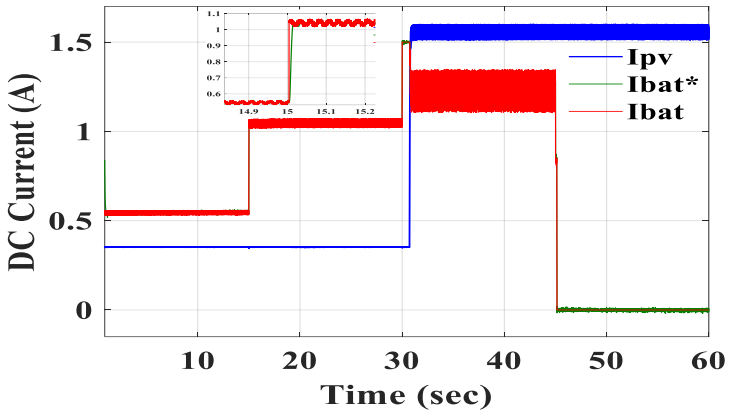

Figure 5.9: PV and battery current response.

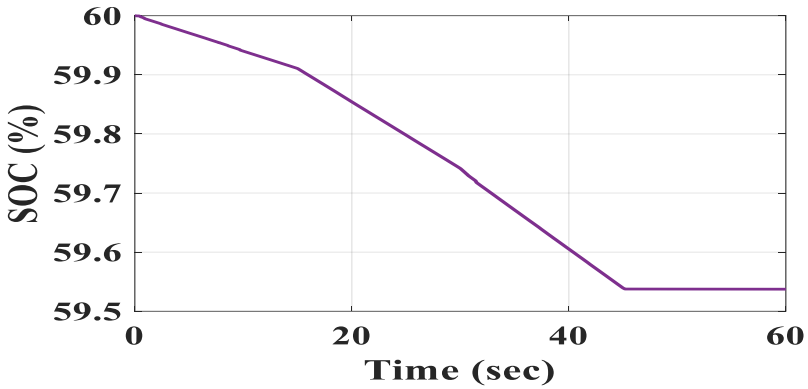

Figure 5.10: Variation in battery SOC.

Figure 5.11 depicts the line current at grid-side. As, power flow is bidirectional in the inverter as well as grid, the direction of this current changes according to EMS.

The formula for load current can be expressed as, $I_{load=}I_{pv} + I_{Bat} + I_g$ (5.1)

Where, I_g is line current at grid-side, which changes according to (5.1). As load is fixed in this test, the load current is constant at 2A given in Figure 5.12. Three-phase currents in Figure 5.10 and 5.11 are presented in zoomed sections for better understanding. Figure 5.13 depicts the DC-link, PV and battery voltages. The DC-link voltage is regulated at a constant 110V, whereas battery and PV voltages are fixed at 48V and 57V respectively. Small overshoots in transition points have appeared in voltage and current signals. In additions, negligible voltage and current ripple can be observed in different operating conditions. The phase voltage of the power grid is around $50V_{peak}$ in the grid-connected microgrid, which is presented in Figure 5.14.

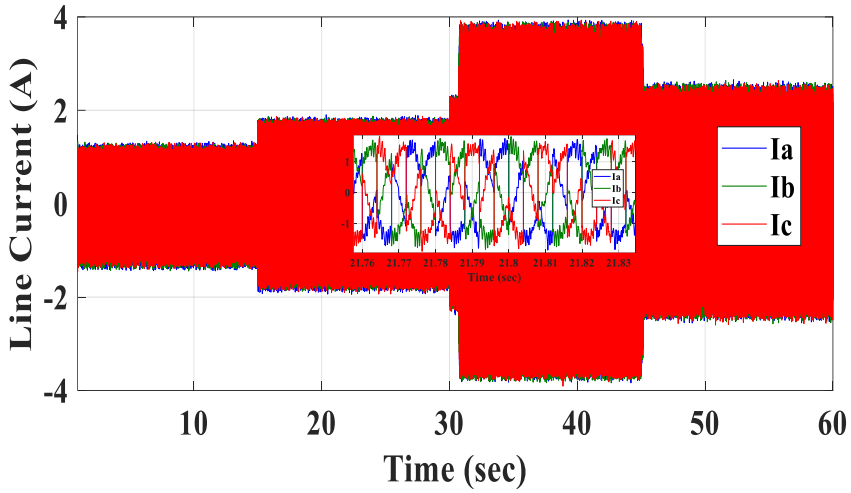

Figure 5.11: Three-phase line current.

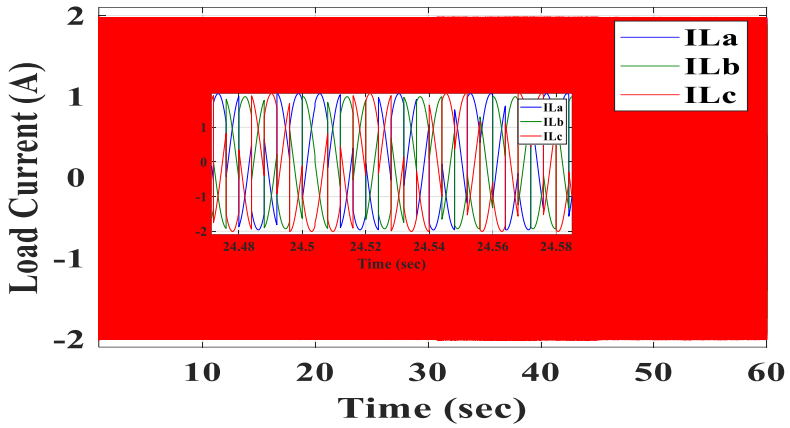

Figure 5.12: Three-phase load current.

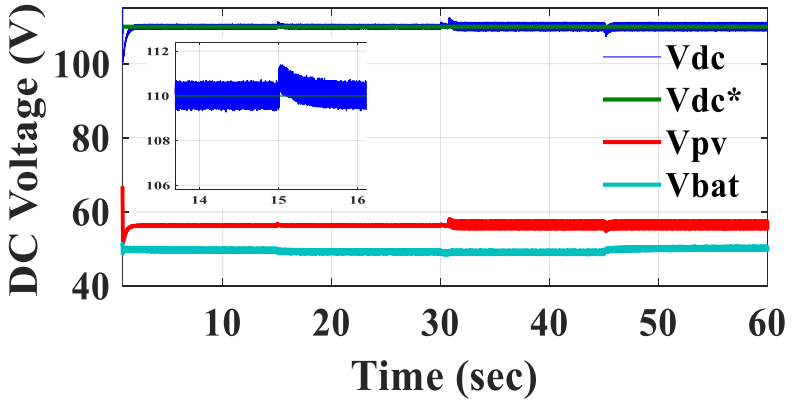

Figure 5.13: PV, battery and DC-link voltage responses.

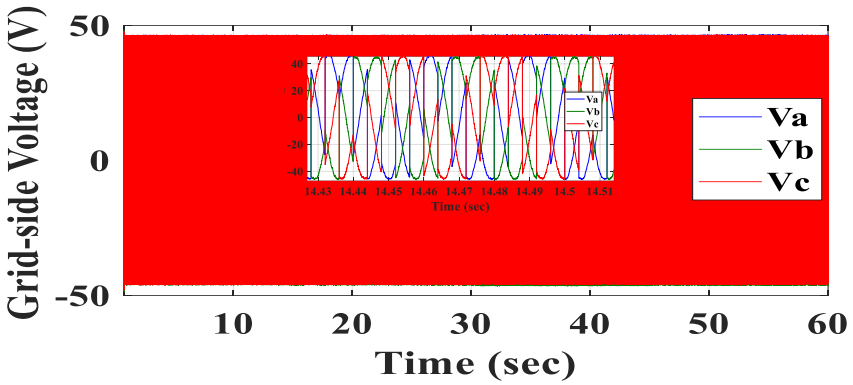

Figure 5.14: Three-phase gird voltage.

5.2.2. EMS Test 2:

In the second execution remaining four operating modes will be tested in t=60sec of run-time. In this execution three conditions: 1) always grid-connected; 2) battery within SOC limit; and 3) PV at MPPT at high irradiance; are always same for all four operating modes.

In Figure 5.15, from t=0 sec to t=30sec, CEM is in operation while the price is at off-peak rate. Due to the off-peak rate, we are trying to consume as much power as possible from the grid. Thus, load demand is served by the PV and grid, besides the battery is charging at its maximum rate. At t=15 sec, EMS switches to PMM, as grid price is at on=peak hour rate. Now, the more we sell the power to grid the more we make profit. In PMM, battery discharges at maximum rate and supplies 50W to the system. In this condition other conditions are remained the same. While grid price is in-between off-peak and on-peak rate, or grid price equals to standard price, then the next two modes will satisfy. EMS checks whether the load demand is higher than PV power, if so, then while load demand higher than at t=30sec IPM activates. To supply the high load battery discharge at an optimum rate by the eqn. (3.8). In contrary to IPM, microgrid generates surplus power when load is less then PV power. At t=45 sec, load demand is deceased to 40W, and the surplus power starts charging the battery using eqn. (3.9).

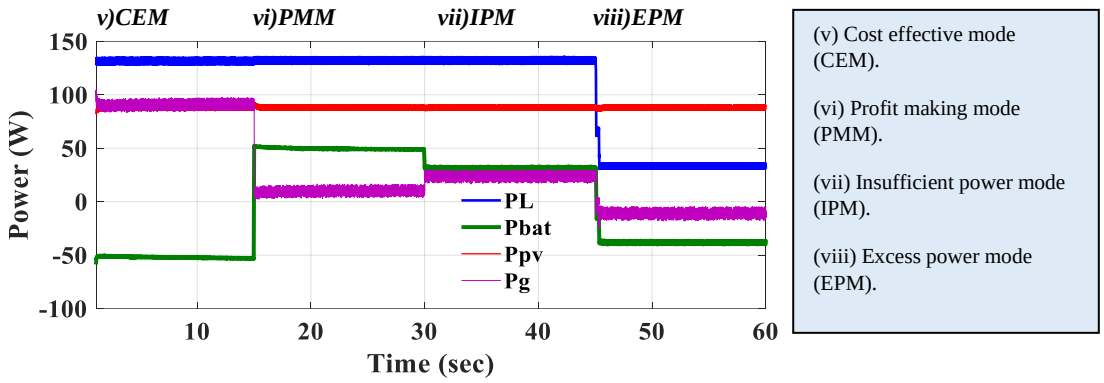

Figure 5.15: Power response in the microgrid system.

Figure 5.16 shows that PV current is fixed at 1.5A for every mode, while battery current follows the battery power. At CEM it charges at a maximum charging current of -1 A, on the hand, at PMM it discharges at a maximum discharging current of 1 A. In next two modes, current charges and discharges at optimal rate according to the power availability. Figure 5.17 shows the change of SOC which exactly follows the battery current. It climbs from 60% to 60.15% at maximum charging, and in the next two modes it discharges to 59.85%. Again, it starts increasing as the system gets surplus power. According to eqn. (5.1) the change in bidirectional line current in grid-side is given in Figure 5.18. As the load is decreased at t=45sec, the change in load current can be observed from Figure 5.19.

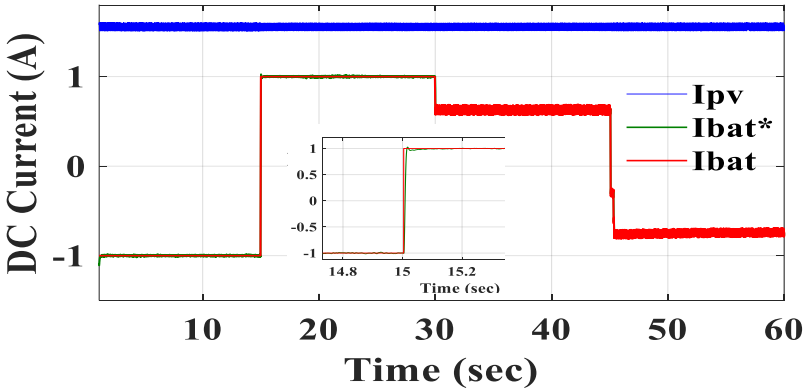

Figure 5.16: PV and battery current response.

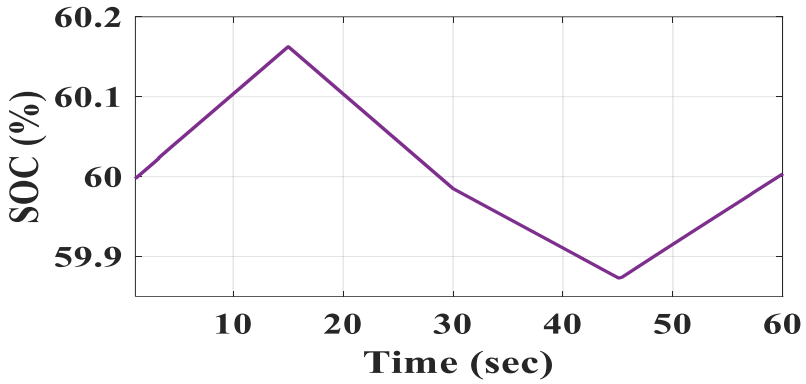

Figure 5.17: Variation in battery SOC.

Figure 5.20 represents the PV, battery and DC-link voltges. Although DC-link voltage is accurately controlled at 110V, negligible overshoots appeared in transision points. The battery, and PV voltage are still constant as the previous test. The test is performed in grid-connected mode, as a result three phase grid voltage is exactly same as previous test.

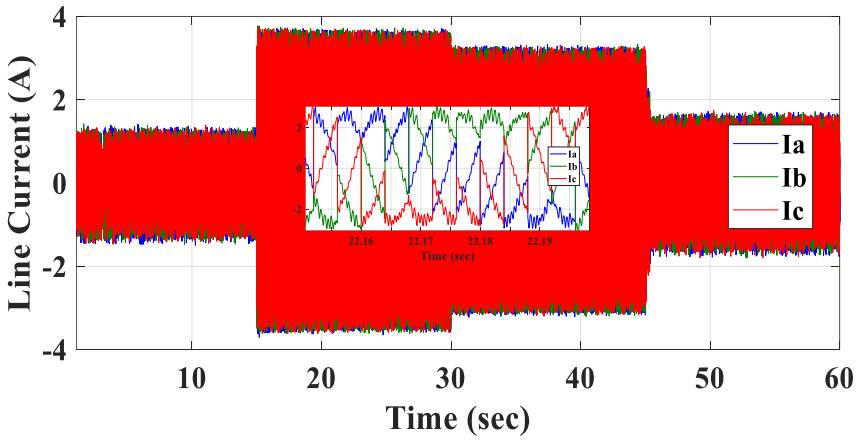

Figure 5.18: Three-phase line current.

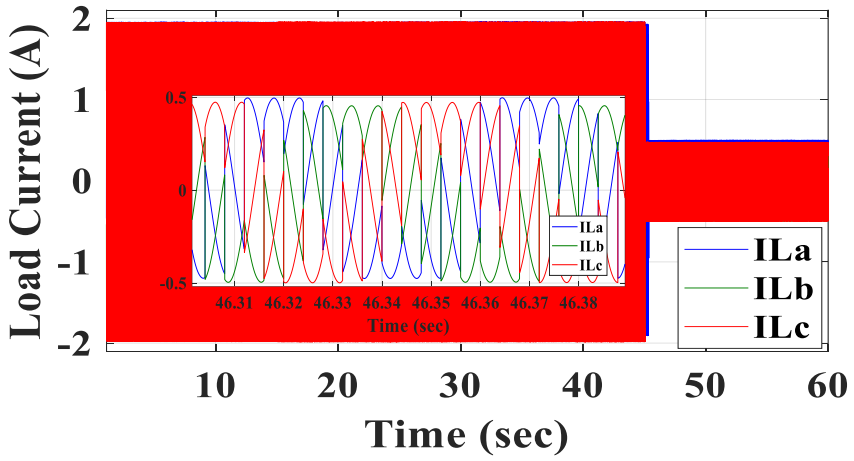

Figure 5.19: Three-phase load current.

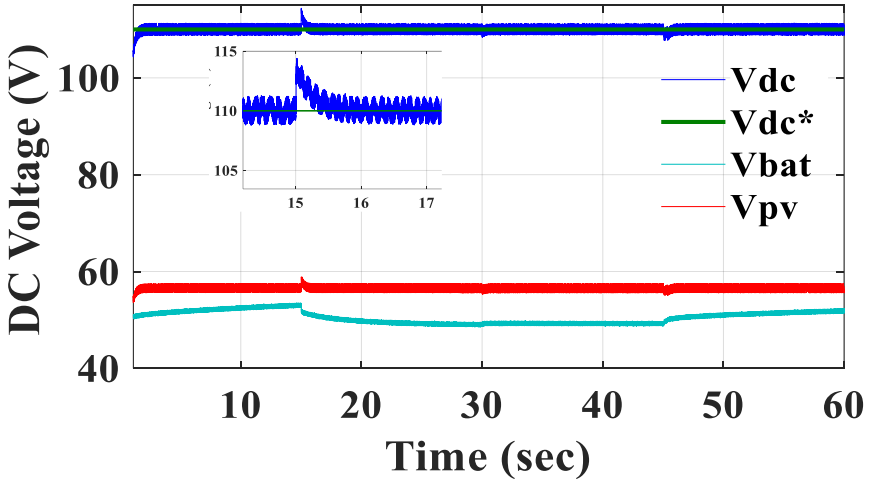

Figure 5.20: PV, battery and DC-link voltage responses.

5.3. Simulation Results and Comparison:

A comparison between hardware set-bed and simulation has been discussed here. An identical Simulink model as the hardware is designed and executed here. The simulation response of EMS of test 1 and test 2 are depicted in Figure 5.21 and Figure 5.22 respectively. The summary of the comparisons is given as follows:

1) In the power response, generated power PV power in simulation is a little bit higher as the PV current is higher. The possible reason is, power losses in filter and other components occur in hardware set-bed. However, seamless transition in both systems is achieved.

Moreover, similar overshoots are experienced in t=30sec where, islanded-mode is activated.

2) The DC-link voltage is well-regulated in both implementations, although PV operating voltage is at 60V which is expected to be at 58V. The capacitor magnetization effect can occur this of small change, however, similar capacitors are used.
3) The voltage ripples in different generating units higher in hardware as it is dealing with physical components. It is noteworthy that physical metering devices are not 100% accurate, that's the reason are getting these negligible mismatches.
4) Other factors such as SOC, line current, load current, are pretty similar in both systems.

So, it can be deduced that the implemented test-bed is accurate enough despite of negligible mismatches. As, the seamless transitions are achieved in both run-times, so it is possible to change the EMS in the modeling and the test-bed would be able to deliver expected results. The Simulink model of the overall system and EMS are provided in the Appendix. C and Appendix. D respectively which can give an understanding of the simulation platform

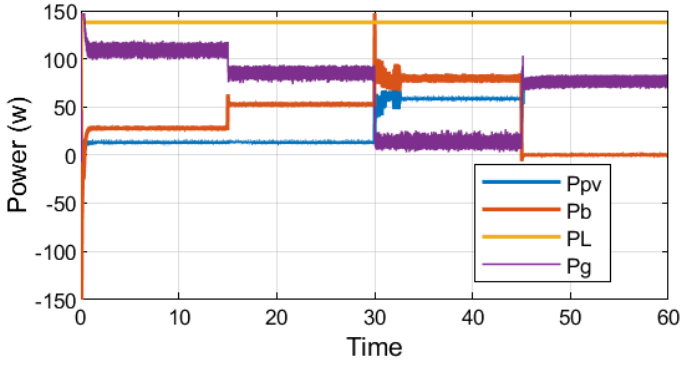

(a)

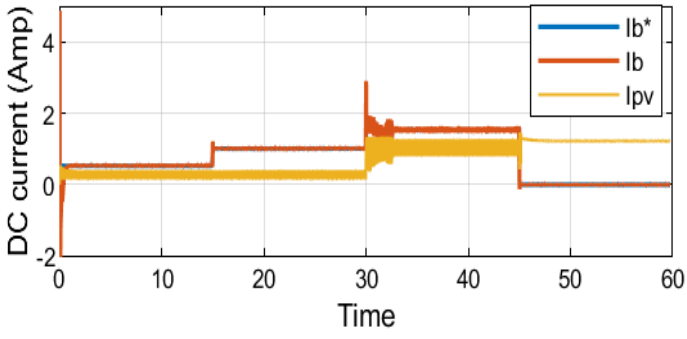

(b)

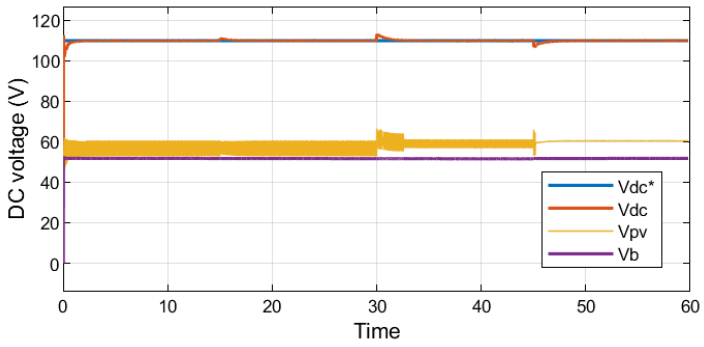
DC voltage (V)
Time
Vdc*
Vdc
Vpv
Vb

(c)

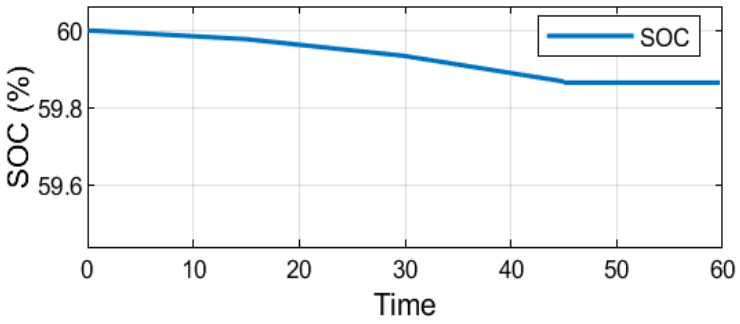
SOC (%)
Time
SOC

(d)

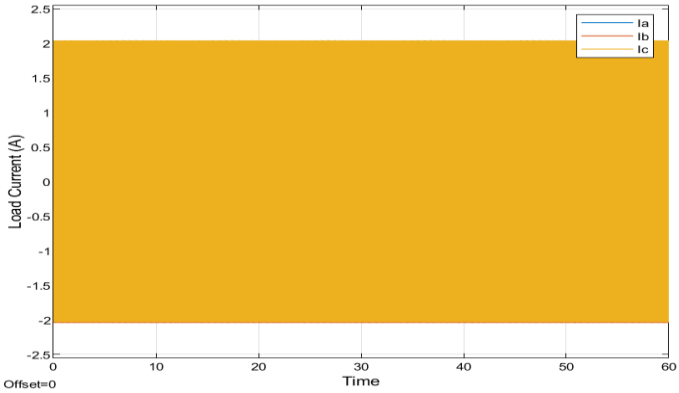
Load Current (A)
Time
Offset=0
Ia
Ib
Ic

(e)

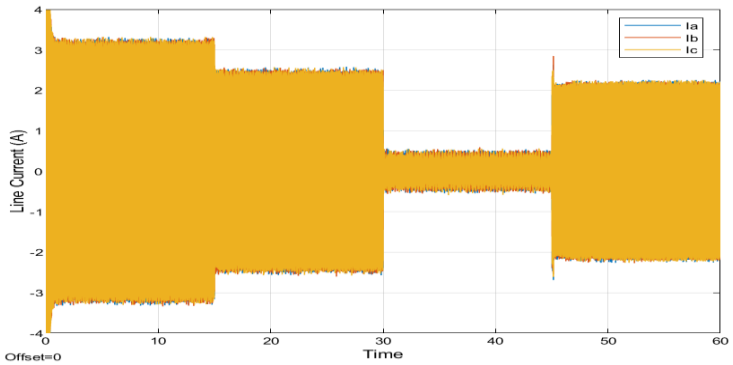

(f)

Figure 5.21: Simulation of EMS test 1-(a) Power responses; (b) PV and battery current; (c) PV, battery and DC-link voltages; (d) change in SOC; (e) load current; (f) line current.

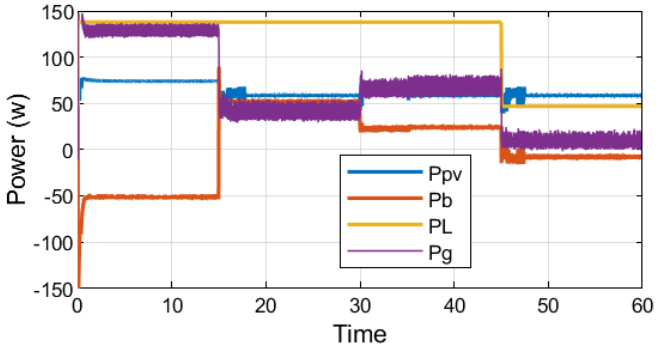

(a)

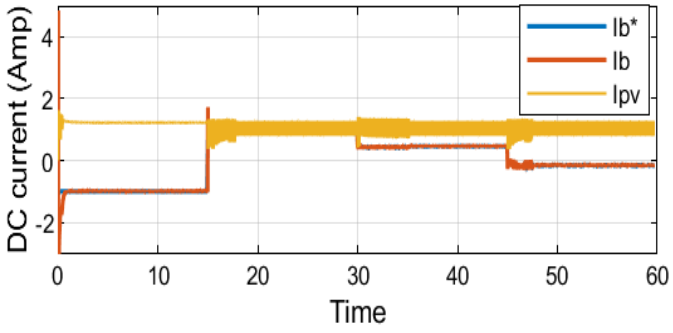

(b)

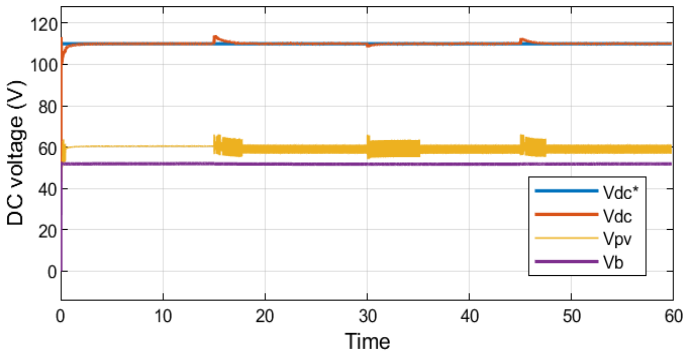
DC voltage (V)
Time
Vdc*
Vdc
Vpv
Vb

(c)

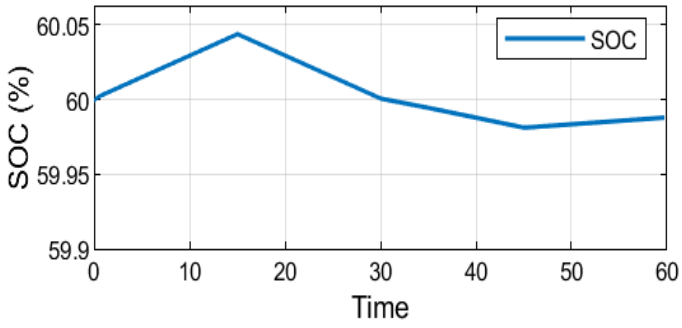
SOC (%)
Time
SOC

(d)

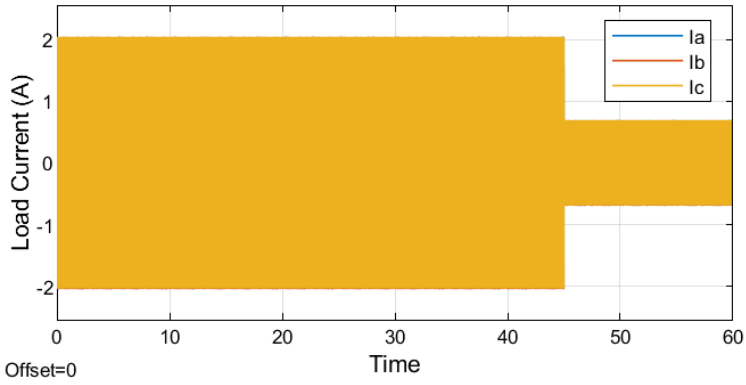
Load Current (A)
Time
Offset=0
Ia
Ib
Ic

(e)

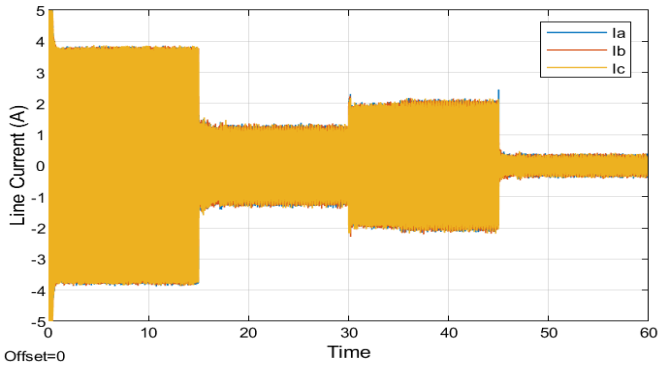

(f)

Figure 5.22: Simulation of EMS test 2-(a) Power responses; (b) PV and battery current; (c) PV, battery and DC-link voltages; (d) change in SOC; (e) load current; (f) line current.

5.4. Conclusion:

This chapter validates the controller design and proposed EMS. The obtained results assure the seamless transition and proper tracking of different operating conditions. In addition, the system gives a prospect of implementing complex EMS and advanced controller in the same test-bed.

Chapter 6: Conclusion and Future Scope

6.1 Conclusion:

The development of microgrid system can be considered as an optimum solution for electrification in rural and isolated regions. In this research project, a PV and battery-storage-based DC-bus microgrid has been introduced. The mathematical formula for the controllers is described. The prime focus of the work is to design and implement a rule-based EMS. The dynamic billing of Nova Scotia, Canada is considered in the EMS. The results from the physical microgrid give an insight into solving the energy crisis in the province. The physical system has taken into consideration efficiency, battery optimal usage and financial benefits. Switching between grid-connected and islanded-mode is a significant feature of the microgrid. For instance, if any microgrid user is not interested in consuming from grid or selling power it can be a right choice for the individual. The EMS can be implemented in different regions in large-scale or in a nano-grid scale. Any system without constraints is unlikely. Instead of using a powerful grid emulator, a Labvolt power supply is used in this work. In additions, some fixed filter circuits are used rather using flexible filters. The microgrid is not operated at the rated power of components, because of limitations of the protective device.

6.2 Future Scope:

The present research work can be extended further. The opportunities for future work include the following,

- Instead of using basic hysteresis controller advanced controllers, for an instant, ANN or fuzzy based controller can be used.
- An adaptive network-based fuzzy inference system (ANFIS) is a kind of artificial neural network which getting popular nowadays. ANFIS-based EMS can be implemented in this system.
- Extensive research in irradiance and load prediction can be examined in this microgrid.
- The system can be reconfigured easily for hybrid (wind, solar and fuel-cell) system or AC-bus microgrid.

Appendix:

A. Perturb & Observe algorithm for MPPT:

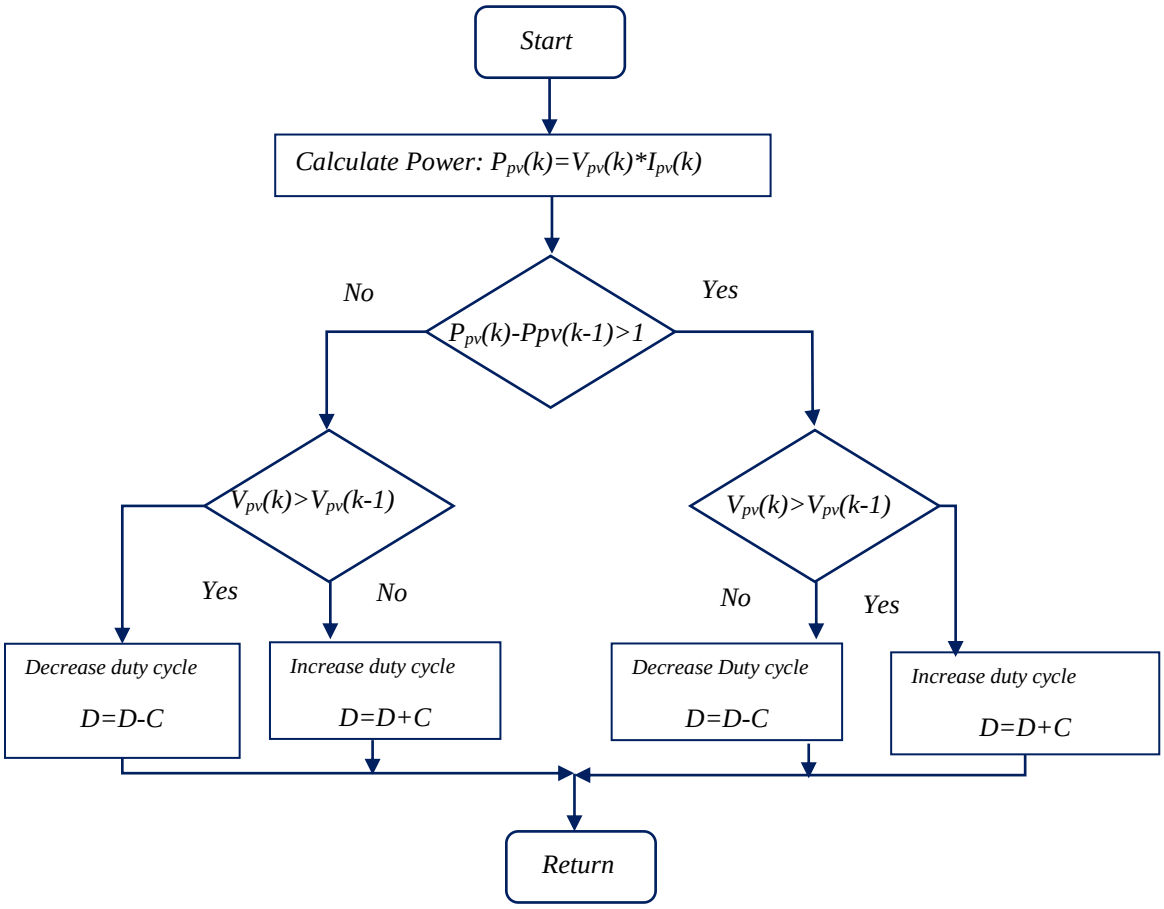

B. Steps for OPAL-RT and RT-Lab executions:

1. Connect OP5600, OP8660, commuter accordingly and install RT-lab software. Connect the PV emulator in the system and install PPPE software.

2. Turn ON the OP5600 Real-time Digital Simulator. And, open RT-LAB in the host computer.

3. Make sure the 'Targets' in 'Project Explorer' window is connected with *LCSM*. To update the connection status, right click on the target *LCSM* and click *Refresh*. In the case of failure to connect, check the blue LAN/Network cable.

4. Create a new RT-LAB Project or access an existing RT-LAB Project (i.e. TEST). Minimize RT-LAB, copy the required basic files, create a new folder (i.e. Control) in the following directory and paste all the files;

Local Disk (C:) > Users> Professor Adel > workspaces > TEST > models > Control

The folder must contain the Simulink model (.mdl) file named *HRES.mdl*, one (.bin) file and one (.conf) file. Both *.bin* and *.conf* files are required to define how the data acquisition read/write channels are assigned.

5. To import Simulink model, double-click on the project, right click on *Models*, go to *Add* select *Existing Model*. From the window click *Import* and select the file from the same directory where the model file (.mdl) was pasted before.

Local Disk (C:) > Users> Professor Adel > workspaces > TEST1 > models > Control

6. Open the RT-LAB window and select the imported file on the project.

7. To apply new control algorithm and modify/update the model, right click on the Simulink model, go to *Edit with* and select *Matlab R2011B (32bit) 7.13.* A new Matlab/Simulink window will appear to apply different control schemes and update the model as desired.

8. Perform the connection depicted between the OP8660 signal conditioning module and Lab-Volt's hardware. Make sure that the plugs of the DB9-8245 encoder cable are correctly connected to their corresponding encoder outputs on the front panel of the 8245 modules.

9. Make sure that the selected converters are fed through its 24V DC input. Turn ON the selected inverter.

10. Turn ON the power input in Magna power DC supply, and open the PPPE software. Prepare the irradiance profiles in PPPE.

11. To compile the simulation model, click on *Build*, make sure the proper Simulink model is selected for compilation.

12. Click on the *Assignation* tab and make sure that the Extra High Performance (XHP) mode in ON. Check the box to turn ON the XHP mode.

13. To upload the model in the real-time simulator, click *Load*. Errors may appear while loading, look for the error description in the *Display* tab and load again after correcting them.

14. If the model is successfully loaded a monitoring console will appear automatically in a new Matlab/Simulink window. The console can be identified by a yellow note titled as *'Automatically generated by RT-LAB during compilation'.*

15. Frist activate the grid power, then PPPE of magna power, then connect battery control.

16. Click *Execute* to run the model. Turn on grid side control then trun on MPPT control.

17. The user console will allow the user to modify the references of the machine during the operation.

18. After completing the execution, the results can be observed from MATLAB workspace.

C. Simulink models of EMS:

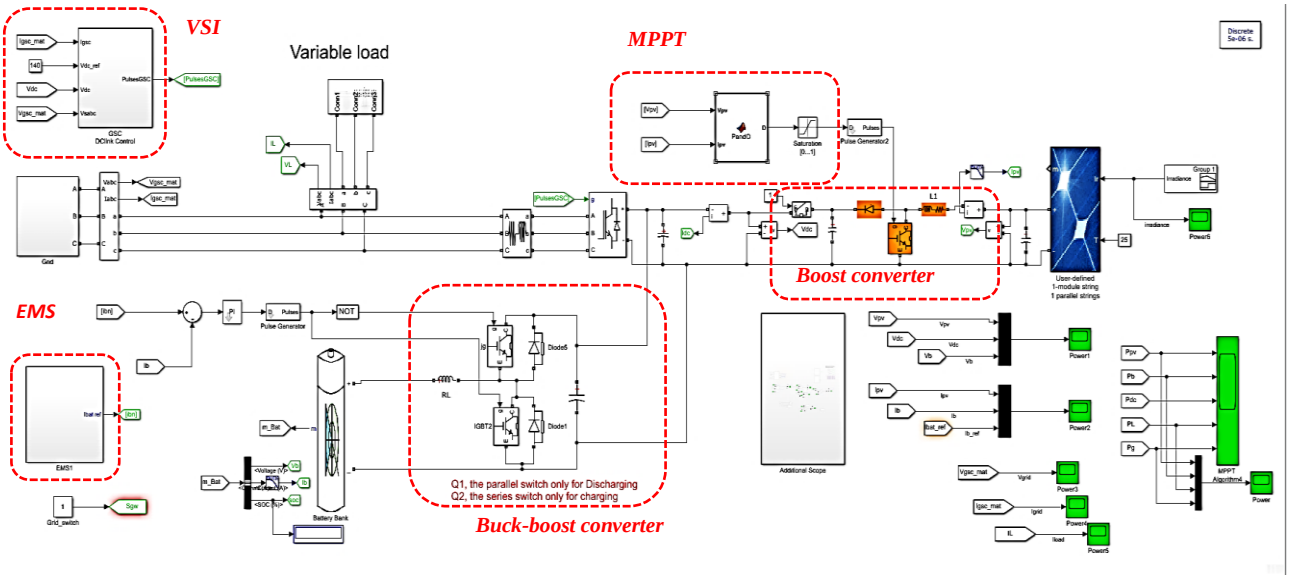

D. Simulink models of EMS:

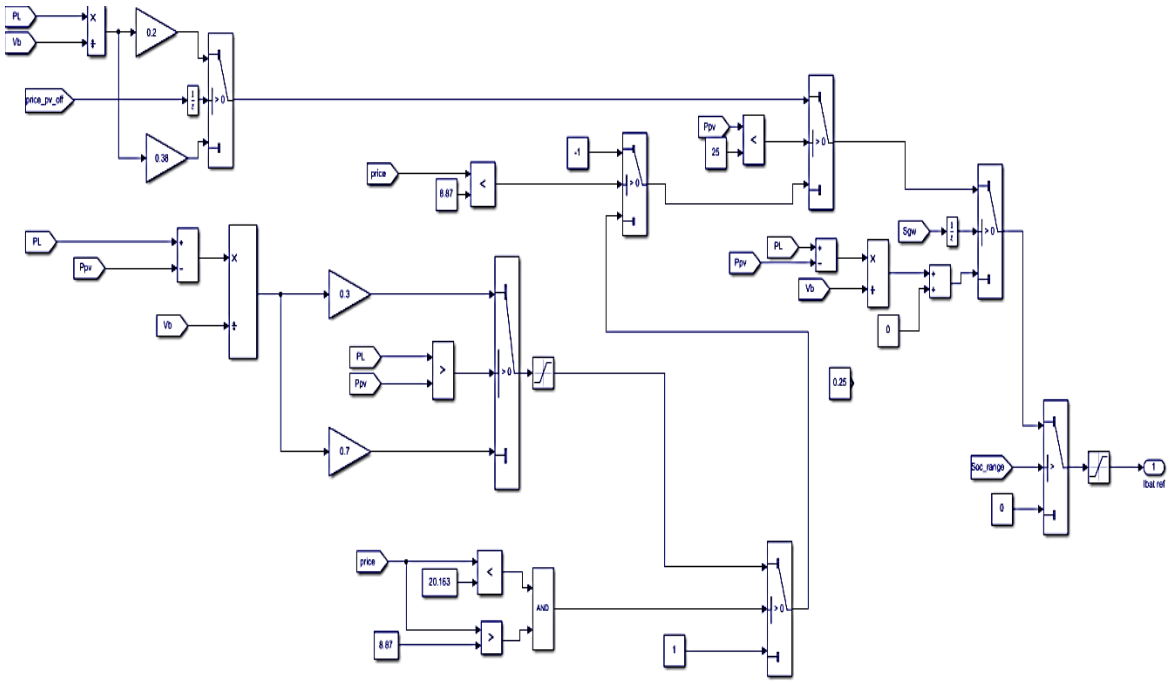

References

[1]. R. Venkatraman and S. K. Khaitan, "A survey of techniques for designing and managing microgrids," *2015 IEEE Power & Energy Society General Meeting, Denver*, CO, 2015, pp. 1-5.

[2]. X. Wang, J. Guerrero, F. Blaabjerg, and Z. Chen, "A Review of PowerElectronic Based Microgrids," *Journal of Power Electronics*, vol. 12, no. 1, pp. 181–192, 2012.

[3]. F. Katiraei, M. R. Iravani, A. L. Dimeas, and N. D. Hatziargyriou, "Microgrids management: control and operation aspects of microgrids," *IEEE Power Energy Mag.*, vol. 6, no. 3, pp. 54–65, May/Jun. 2008.

[4]. P. Dondi, D. Bayoumi, C. Haederli, D. Julian, and M. Suter, "Network integration of distributed power generation," *J. of Power Sources*, vol, 106, no. 1–2, pp. 1–9, 2002.

[5]. D. E. Olivares et al., "Trends in Microgrid Control," *IEEE Trans. Smart Grid*, vol. 5, no. 4, pp. 1905-1919, July 2014.

[6]. N. Ruiz, I. Cobelo, and J. Oyarzabal, "A direct load control model for virtual power plant management," *IEEE Trans. Power Syst.*, vol. 24, no. 2, pp. 959–966, May 2009.

[7]. D. Pudjianto, C. Ramsay, and G. Strbac, "Virtual power plant and system integration of distributed energy resources," *IET Renew. Power Gener*., vol. 1, no. 1, pp. 10–16, Mar. 2007.

[8]. R. Palma-Behnke, C. Benavides, F. Lanas, B. Severino, L. Reyes, J. Llanos, and D. Sáez, "A microgrid energy management system based on the rolling horizon strategy," *IEEE Trans. Smart Grid*, vol. 4, no. 2, pp. 996–1006, Jun. 2013.

[9]. Y. A.-R. I. Mohamed and A. A. Radwan, "Hierarchical control system for robust microgrid operation and seamless mode transfer in active distribution systems," *IEEE Trans. Smart Grid*, vol. 2, no. 2, pp. 1949–3053, Jun. 2011.

[10]. A. Mehrizi-Sani and R. Iravani, "Potential-function based control of a microgrid in islanded and grid-connected modes," *IEEE Trans. Power Syst.*, vol. 25, no. 4, pp. 1883–1891, Nov. 2010.

[11]. F. Blaabjerg, R. Teodorescu, M. Liserre, and A. V. Timbus, "Overview of control and grid synchronization for distributed power generation systems," *IEEE Trans. Ind. Electron.*, vol. 53, no. 5, pp. 1398–1409, Oct. 2006.

[12]. J. Kim, J. M. Guerrero, P. Rodriguez, R. Teodorescu, and K. Nam, "Mode adaptive droop control with virtual output impedances for an inverter-based flexible AC microgrid," *IEEE Trans. Power Electron*., vol. 26, no. 3, pp. 689–701, Mar. 2011.

[13]. M. B. Delghavi and A. Yazdani, "An adaptive feedforward compensation for stability enhancement in droop-controlled inverter-based microgrids," *IEEE Trans. Power Del*., vol. 26, no. 3, pp. 1764–1773, Jul. 2011.

[14]. R. Majumder, B. Chaudhuri, A. Ghosh, R.Majumder, G. Ledwich, and F. Zare, "Improvement of stability and load sharing in an autonomous microgrid using supplementary droop control loop," *IEEE Trans. Power Syst.*, vol. 25, no. 2, pp. 796–808, May 2010.

[15]. C.-L. Chen, Y. Wang, J.-S. Lai, Y.-S. Lee, and D. Martin, "Design of parallel inverters for smooth mode transfer microgrid applications," *IEEE Trans. Power Electron*., vol. 25, no. 1, pp. 6–15, Jan.2010.

[16]. J.M.Guerrero, L. Hang, and J. Uceda, "Control of distributed uninterruptible power supply systems," *IEEE Trans. Ind. Electron*., vol. 55, no. 8, pp. 2845–2859, Aug. 2008.

[17]. C. Schwaegerl, L. Tao, P. Mancarella, and G. Strbac, "A multi-objective optimization approach for assessment of technical, commercial and environmental performance of microgrids," *Eur. Transact. on Electrical Power*, vol. 21, no. 2, pp. 1269–1288, 2011.

[18]. M. R. D. Zadeh, A. Hajimiragha, M. Krok, S. Allan, and A. Palizban, "Bella Coola microgrid generation optimization with a hydro-electric unit operating in isochronous mode," *in Proc. CIGRE,* Sep. 2011.

[19]. L. Xiaoping, D. Ming, H. Jianghong, H. Pingping and P. Yali, "Dynamic economic dispatch for microgrids including battery energy storage," *The 2nd International Symposium on Power Electronics for Distributed Generation Systems, Hefei*, 2010, pp. 914-917.

[20]. F. Nejabatkhah and Y. W. Li, "Overview of Power Management Strategies of Hybrid AC/DC Microgrid," *IEEE Trans. Power Electron*., vol. 30, no. 12, pp. 7072-7089, Dec. 2015.

[21]. T. Logenthiran, D. Srinivasan and D. Wong, "Multi-agent coordination for DER in MicroGrid," *2008 IEEE International Conference on Sustainable Energy Technologies*, Singapore, 2008, pp. 77-82.

[22]. P. Tenti and T. Caldognetto, "On Microgrid Evolution to Local Area Energy Network (E-LAN)," *IEEE Trans. Smart Grid, vol*. 10, no. 2, pp. 1567-1576, March 2019.

[23]. T. Dragičević, X. Lu, J. C. Vasquez and J. M. Guerrero, "DC Microgrids—Part I: A Review of Control Strategies and Stabilization Techniques," *IEEE Trans. Power Electron*., vol. 31, no. 7, pp. 4876-4891, July 2016.

[24]. B. M. Eid, N. A. Rahim, J. Selvaraj and A. H. El Khateb, "Control Methods and Objectives for Electronically Coupled Distributed Energy Resources in Microgrids: A Review," *IEEE Sys. Journal*, vol. 10, no. 2, pp. 446-458, June 2016.

[25]. L. Igualada, C. Corchero, M. Cruz-Zambrano and F. -. Heredia, "Optimal Energy Management for a Residential Microgrid Including a Vehicle-to-Grid System," *IEEE Trans. Smart Grid*, vol. 5, no. 4, pp. 2163-2172, July 2014.

[26]. F. Gomez-Cuba, R. Asorey-Cacheda and F. J. Gonzalez-Castano, "Smart Grid Last-Mile Communications Model and Its Application to the Study of Leased Broadband Wired-Access," *IEEE Trans. Smart Grid*, vol. 4, no. 1, pp. 5-12, March 2013.

[27]. A. G. Tsikalakis and N. D. Hatziargyriou, "Centralized control for optimizing microgrids operation," *2011 IEEE Power and Energy Society General Meeting, Detroit, MI, USA*, 2011, pp. 1-8.

[28]. M. Manbachi and M. Ordonez, "AMI-Based Energy Management for Islanded AC/DC Microgrids Utilizing Energy Conservation and Optimization," *IEEE Trans. Smart Grid*, vol. 10, no. 1, pp. 293-304, Jan. 2019.

[29]. N. Tiwari and L. Srivastava, "Generation scheduling and micro-grid energy management using differential evolution algorithm," *2016 International Conference on Circuit, Power and Computing Technologies (ICCPCT), Nagercoil*, 2016, pp. 1-7.

[30]. M. Marzband, F. Azarinejadian, M. Savaghebi and J. M. Guerrero, "An Optimal Energy Management System for Islanded Microgrids Based on Multiperiod Artificial Bee Colony Combined With Markov Chain," *IEEE Sys. Journal*, vol. 11, no. 3, pp. 1712-1722, Sept. 2017.

[31]. B. Papari, C. S. Edrington, T. V. Vu and F. Diaz-Franco, "A heuristic method for optimal energy management of DC microgrid," *2017 IEEE Second International Conference on DC Microgrids (ICDCM), Nuremburg*, 2017, pp. 337-343.

[32]. K. Huang, X. Wang and L. Wang, "Optimal energy management of grid-connected photovoltaic micro-grid," *2015 IEEE International Conference on Cyber Technology in Automation, Control, and Intelligent Systems (CYBER), Shenyang*, 2015, pp. 234-239.

[33]. Y. Chen, Y. Wu, C. Song and Y. Chen, "Design and Implementation of Energy Management System With Fuzzy Control for DC Microgrid Systems," *IEEE Trans. Power Electron.*, vol. 28, no. 4, pp. 1563-1570, April 2013.

[34]. H. S. V. S. Kumar Nunna and S. Doolla, "Energy Management in Microgrids Using Demand Response and Distributed Storage—A Multiagent Approach," *IEEE Trans. Power Del*., vol. 28, no. 2, pp. 939-947, April 2013.

[35]. M. E. Gamez Urias, E. N. Sanchez and L. J. Ricalde, "Electrical Microgrid Optimization via a New Recurrent Neural Network," *IEEE Sys. Journal*, vol. 9, no. 3, pp. 945-953, Sept. 2015.

[36]. G. E. Asimakopoulou, A. L. Dimeas and N. D. Hatziargyriou, "Leader-Follower Strategies for Energy Management of Multi-Microgrids," *IEEE Trans. Smart Grid*, vol. 4, no. 4, pp. 1909-1916, Dec. 2013.

[37]. L. I. Minchala-Avila, L. Garza-Castañon, Y. Zhang and H. J. A. Ferrer, "Optimal Energy Management for Stable Operation of an Islanded Microgrid," *IEEE Trans. Ind. Info.*, vol. 12, no. 4, pp. 1361-1370, Aug. 2016.

[38]. B. V. Solanki, K. Bhattacharya and C. A. Cañizares, "A Sustainable Energy Management System for Isolated Microgrids," *IEEE Trans. Sustain. Energy*, vol. 8, no. 4, pp. 1507-1517, Oct. 2017.

[39]. B. Kroposki, R. Lasseter, T. Ise, S. Morozumi, S. Papathanassiou and N. Hatziargyriou, "Making microgrids work," *IEEE Power and Energy Magazine*, vol. 6, no. 3, pp. 40-53, May-June 2008.

[40]. F. Katiraei, C. Abbey, S. Tang and M. Gauthier, "Planned islanding on rural feeders — utility perspective," *2008 IEEE Power and Energy Society General Meeting - Conversion and Delivery of Electrical Energy in the 21st Century, Pittsburgh, PA*, 2008, pp. 1-6.

[41]. E. Joseph, R. Lasseter, B. Schenkman, J. Stevens, H. Volkommer, and D. Klapp, "CERTS microgrid laboratory Testbed. Consortium for Electric Reliability Technology Solutions (CERTS)," *California Energy Commission, Public Interest Energy Research Program, CEC*-500-2008-XXX; 2008.

[42]. T. Loix, and K.Leuven, "The first micro grid in the Netherlands: Bronsbergen,"Available online on June 2020. http://www.leonardo-energy.org/webfm_send/493 .

[43]. M. Barnes et al., "Microgrid laboratory facilities," *2005 International Conference on Future Power Systems, Amsterdam,* 2005, pp. 6 pp.-6.

[44]. T. Shimakage, Jiro Sumita, Noriyuki Uchiyama, T. Kato and Y. Suzuoki, "Supply and demand control of distributed generators in a microgrid," *INTELEC 2008 - 2008 IEEE 30th International Telecommunications Energy Conference, San Diego, CA,* 2008, pp. 1-5.

[45]. H. Hatta and H. Kobayashi, "Demonstration study on centralized voltage control system for distribution line with sudden voltage fluctuations," *CIRED Seminar 2008: SmartGrids for Distribution, Frankfurt,* 2008, pp. 1-4.

[46]. R. N. Ray, D. Chatterjee and S. K. Goswami, "Reduction of voltage harmonics using optimisation-based combined approach," *IET Power Elect.,* vol. 3, no. 3, pp. 334-344, May 2010.

[47]. P. Shah, I. Hussain, B. Singh, A. Chandra and K. Al-Haddad, "GI-Based Control Scheme for Single-Stage Grid Interfaced SECS for Power Quality Improvement," *IEEE Trans. Ind. Appl.*, vol. 55, no. 1, pp. 869-881, Jan.-Feb. 2019.

[48]. S. Pradhan, I. Hussain, B. Singh and B. Ketan Panigrahi, "Performance Improvement of Grid-Integrated Solar PV System Using DNLMS Control Algorithm," *IEEE Trans. Ind. Appl.*, vol. 55, no. 1, pp. 78-91, Jan.-Feb. 2019.

[49]. V. Jain and B. Singh, "A Multiple Improved Notch Filter-Based Control for a Single-Stage PV System Tied to a Weak Grid," *IEEE Trans. Sustain.. Energy,* vol. 10, no. 1, pp. 238-247, Jan. 2019.

[50]. S. Kotra and M. K. Mishra, "A Supervisory Power Management System for a Hybrid Microgrid With HESS," *IEEE Trans. Ind. Electron.*, vol. 64, no. 5, pp. 3640-3649, May 2017.

[51]. J. Schonbergerschonberger, R. Duke and S. D. Round, "DC-Bus Signaling: A Distributed Control Strategy for a Hybrid Renewable Nanogrid," *IEEE Trans. Ind. Electron.*, vol. 53, no. 5, pp. 1453-1460, Oct. 2006.

[52]. H. Liang, B. J. Choi, W. Zhuang and X. Shen, "Stability Enhancement of Decentralized Inverter Control Through Wireless Communications in Microgrids," *IEEE Trans. Smart Grid*, vol. 4, no. 1, pp. 321-331, March 2013.

[53]. K. Sun, L. Zhang, Y. Xing and J. M. Guerrero, "A Distributed Control Strategy Based on DC Bus Signaling for Modular Photovoltaic Generation Systems With Battery Energy Storage," *IEEE Trans. Power Electron.*, vol. 26, no. 10, pp. 3032-3045, Oct. 2011.

[54]. H. Yin, W. Zhou, M. Li, C. Ma and C. Zhao, "An Adaptive Fuzzy Logic-Based Energy Management Strategy on Battery/Ultracapacitor Hybrid Electric Vehicles," *IEEE Trans. Trans. Electrification*, vol. 2, no. 3, pp. 300-311, Sept. 2016.

[55]. X. Feng, H. B. Gooi and S. X. Chen, "Hybrid Energy Storage With Multimode Fuzzy Power Allocator for PV Systems," *IEEE Trans. Sustain. Energy*, vol. 5, no. 2, pp. 389-397, April 2014.

[56]. N. Chettibi, A. Mellit, G. Sulligoi and A. Massi Pavan, "Adaptive Neural Network-Based Control of a Hybrid AC/DC Microgrid," *IEEE Trans. Smart Grid*, vol. 9, no. 3, pp. 1667-1679, May 2018.

[57]. S. Kotra and M. K. Mishra, "A Supervisory Power Management System for a Hybrid Microgrid With HESS," *IEEE Trans. Ind. Electron.*, vol. 64, no. 5, pp. 3640-3649, May 2017.

[58]. N. Korada and M. K. Mishra, "Grid Adaptive Power Management Strategy for an Integrated Microgrid With Hybrid Energy Storage," *IEEE Trans. Ind. Electron.*, vol. 64, no. 4, pp. 2884-2892, April 2017.

[59]. P. P. Vergara, J. C. López, M. J. Rider and L. C. P. da Silva, "Optimal Operation of Unbalanced Three-Phase Islanded Droop-Based Microgrids," *IEEE Trans. Smart Grid*, vol. 10, no. 1, pp. 928-940, Jan. 2019.

[60]. R. K. Dhar, A. Merabet, A. M. Y. M. Ghias and Z. Qin, "Control Architecture of Solar Photovoltaic AC-Bus Microgrid with Battery Storage System," *2019 IEEE 28th International Symposium on Industrial Electronics (ISIE)*, Vancouver, BC, Canada, 2019, pp. 1072-1077.

[61]. H. E. Toosi, A. Merabet, A. M. Y. M. Ghias and A. Swingler, "Central Power Management System for Hybrid PV/Battery AC-Bus Microgrid Using Typhoon HIL," *2019 IEEE 28th International Symposium on Industrial Electronics (ISIE)*, Vancouver, BC, Canada, 2019, pp. 1053-1058.

[62]. A. Merabet and R. K. Dhar, "Solar Photovoltaic Microgrid Simulation Platform for Energy Management Testing," *2019 Algerian Large Electrical Network Conference (CAGRE)*, Algiers, Algeria, 2019, pp. 1-5.

[63]. H. Yang, W. Zhou, L. Lu, and Z. Fang, "Optimal sizing method for stand-alone hybrid solar–wind system with LPSP technology by using genetic algorithm," *Elsevier Journal of Solar Energy*, vol. 82, pp. 354-367, Aug. 2007.

[64]. B. O. Bilal, V. Sambou, P. A. Ndiaye, C. M. Kebe, and M. Ndongo "Optimal design of a hybrid solar–wind-battery system using the minimization of the annualized cost system and the minimization of the loss of power supply probability (LPSP)," *Elsevier Journal of Renewable Energy*, vol. 35, no. 10, pp. 2388-2390, Oct. 2010.

[65]. O. Ekren and B. Y. Ekren, "Size optimization of a PV/wind hybrid energy conversion system with battery storage using response surface methodology," *Journal of Applied Energy*, vol. 85, no. 11, pp. 1086 – 1101, Feb. 2008.

[66]. H. R. Baghaee, M. Mirsalim, and G. B. Gharehpetian, "Multiobjective optimal power management and sizing of a reliable Wind/PV microgrid with hydrogen energy storage using MOPSO," *Journal of Intelligent & Fuzzy Systems*, vol. 32, no. 3, pp. 1753-1773, Feb. 2017.

[67]. S. Mirjalili and S. Z. M. Hashim, "A new hybrid PSOGSA algorithm for function optimization," *2010 International Conference on Computer and Information Application, Tianjin*, 2010, pp. 374-377.

[68]. H. Myneni and G. Siva Kumar, "Energy Management and Control of Single-Stage Grid Connected Solar PV and BES System," *IEEE Trans. Sustain. Energy*, vol. PP, no. c, pp. 1–1, 2019.

[69]. U. Manandhar et al., "Energy management and control for grid connected hybrid energy storage system under different operating modes," *IEEE Trans. Smart Grid*, vol. 10, no. 2, pp. 1626–1636, 2019.

[70]. J. He, Y. Li, C. Wang, Y. Pan, C. Zhang, and X. Xing, “Hybrid Microgrid with Parallel-and Series-Connected Microconverters,” *IEEE Trans. Power Electron*., vol. 33, no. 6, pp. 4817–4831, 2018.

[71]. Y. Yang, Q. Ye, L. J. Tung, M. Greenleaf, and H. Li, “Integrated Size and Energy Management Design of Battery Storage to Enhance Grid Integration of Large-Scale PV Power Plants,” *IEEE Trans. Ind. Electron*., vol. 65, no. 1, pp. 394–402, 2018.

[72]. Z Almukhtar, A Merabet, “Maximum Power Point Tracking Based on Estimated Power for PV Energy Conversion System,” *International Journal of Electrical, Computer, Energetic, Electronic and Communication Engineering*, vol. 10, pp. 573-577, Aug. 2017.

[73]. MA Islam, A Merabet, R Beguenane, H Ibrahim, H Ahmed, “Simulation based study of Maximum Power Point Tracking and Frequency Regulation for Stand-alone Solar Photovoltaic Systems,” *International Conference on Renewable Energies and Power Quality (ICREPQ’14)*, Codoba, Spain, 8-10 April 2014.

[74]. J. Ahmed and Z. Salam, “A Modified P and O Maximum Power Point Tracking Method with Reduced Steady-State Oscillation and Improved Tracking Efficiency,” *IEEE Trans. Sustain. Energy*, vol. 7, no. 4, pp. 1506–1515, 2016.

[75]. L. Labib, A. Merabet and A. M. Y. M. Ghias, "Low-Voltage Ride-Through Operation of Permanent Magnet Synchronous Generator with Active and Reactive Power Injection," *IECON 2018 - 44th Annual Conference of the IEEE Industrial Electronics Society, Washington, DC*, 2018, pp. 1848-1853.

[76]. A. Merabet, L. Labib and A. M. Y. M. Ghias, "Robust Model Predictive Control for Photovoltaic Inverter System With Grid Fault Ride-Through Capability," *IEEE Trans. Smart Grid*, vol. 9, no. 6, pp. 5699-5709, Nov. 2018.

[77]. D. P. Hohm and M. E. Ropp, "Comparative study of maximum power point tracking algorithms using an experimental, programmable, maximum power point tracking test bed," *in Photovoltaic Specialists Conference, 2000. Conference Record of the Twenty-Eighth IEEE*, 2000, pp. 1699-1702.

[78]. V. Salas, E. Olías, A. Barrado and A. Lázaro, "Review of the maximum power point tracking algorithms for stand-alone photovoltaic systems," *Solar Energy Mater. Solar Cells,* vol. 90, pp. 1555-1578, 7/6, 2006.

[79]. A Merabet, L Labib, AMYM Ghias, A Al-Durra, M Debbouza, "Dual-mode operation based second-order sliding mode control for grid-connected solar photovoltaic energy system, " *International Journal of Electrical Power & Energy Systems*, vol. 111, pp. 459-474, Oct. 2019.

[80]. A. Merabet, L. Labib, A. M. Y. M. Ghias, C. Ghenai and T. Salameh, "Robust Feedback Linearizing Control With Sliding Mode Compensation for a Grid-Connected Photovoltaic Inverter System Under Unbalanced Grid Voltages," *IEEE Journal of Photovoltaics*, vol. 7, no. 3, pp. 828-838, May 2017.

[81]. Y. Nakata, K. Fujiwara, M. Yoshida, J. Itoh and Y. Okazaki, "Output voltage control for PWM inverter with electric double layer capacitor as DC power supply," *Power Electronics Conference (IPEC), 2010 International,2010*, pp. 3099-3104.

[82]. A. Meskani, A. Haddi and M. Becherif, "Modeling and simulation of a hybrid energy source based on solar energy and battery," *Int J Hydrogen Energy*, vol. 40, pp. 13702-13707, 10/19, 2015.

[83]. J. Appelbaum and R. Weiss, "An electrical model of the lead-acid battery," Telecommunications *Energy Conference, 1982. INTELEC 1982. International,* 1982, pp. 304-307.

[84]. H. He, R. Xiong and J. Fan, "Evaluation of Lithium-Ion Battery Equivalent Circuit Models for State of Charge Estimation by an Experimental Approach," *Energies*, vol. 4, pp. 582-598, 2011.

[85]. R. K. Soni, A. K. Chauhan, R. R. Kumar and S. K. Singh, "Comparative study of SVM and hysteresis control strategies for grid side converter of PMSG," *Annual IEEE India Conference (INDICON), Pune*, pp. 1-6, 2014.

[86]. J. Eloy-Garcia, S. Arnaltes and J. L. Rodriguez-Amenedo, "Direct power control of voltage source inverters with unbalanced grid voltages," *IET Power Electronics*, vol. 1, no. 3, pp. 395-407, 2008.

[87]. Z Almukhtar, A Merabet, "Fuzzy MPPT Control and Power Regulation for Standalone Photovoltaic Energy Conversion System," *International Journal of Advanced Engineering Research and Applications*, vol. 2, no. 7, pp. 371-381, Nov. 2016.

[88]. A Merabet, Q Zhang, AMYM Ghias, “Control of Simulated Solar PV Microgrid Operating in Grid-Tied and Islanded Modes,” *IECON 2018 44th Annual Conference of the IEEE Industrial Electronics Society*, Washington, DC, USA, pp. 21-23 Oct. 2018.

[89]. MA Islam, A Merabet, R Beguenane, H Ibrahim, Modeling solar photovoltaic cell and simulated performance analysis of a 250W PV module, 2013 IEEE Electrical Power & Energy Conference, pp. 1-6, Aug. 2013.

[90]. J. Mohammadi, S. Vaez-Zadeh, S. Afsharnia and E. Daryabeigi, "A Combined Vector and Direct Power Control for DFIG-Based Wind Turbines," *IEEE Trans. Sustain. Energy*, vol. 5, no. 3, pp. 767-775, 2014.

[91]. H. Hasanien, M. Matar, “Water Cycle Algorithm-based Optimal Control Strategy for Efficient Operation of an Autonomous Microgrid’,’ *IET Generation, Transmission & Distribution*, 2018.

[92]. H. Eskandar, A. Sadollah, A. Bahreininejad, M. Hamdi “Water cycle algorithm – A novel metaheuristic optimization method for solving constrainted engineering optimization problems,” *Comput. Struct.*, vol. 110–111, pp. 151–166, 2012.

[93]. (2020) Nova Scotia Power. [Online]. Available: https://www.nspower.ca/

[94]. A. Merabet, K. T. Ahmed, H. Ibrahim, R. Beguenane, and A. M. Y. M. Ghias, “Energy management and control system for laboratory scale microgrid based wind- PV-battery,” *IEEE Trans. Sustain. Energy*, vol. 8, no. 1, pp. 145–154, Jan 2017.

[95]. P. V. J. Belanger and J. N. Paquin, The What, Where, and Why of Real Time Simulation. *OPAL-RT Publication, 2010.*

[96]. K. A. Tawfique, A. Merabet, H. Ibrahim and R. Beguenane, "Standalone wind energy conversion system using OPAL-RT real-time HIL/RCP laboratory," *2016 International Conference on Industrial Informatics and Computer Systems (CIICS), Sharjah*, 2016, pp. 1-5.

[97]. P. M. Menghal and A. J. Laxmi, “Real time simulation: A novel approach in engineering education,” *2011 3rd International Conference on Electronics Computer Technology*, vol. 1, April 2011, pp. 215–219.

[98]. (2017) Real-time simulation. [Online]. Available: http://www.opalrt.com/training-programs-overview/.

[99]. MA Islam, A Merabet, R Beguenane, H Ibrahim, “Power management strategy for solar-wind-diesel stand-alone hybrid energy system,” *International Journal of Energy and Power Engineering*, vol. 8, no.6, pp.850-85, 2014.

[100]. KT Ahmed, A Merabet, R Beguenane, H Ibrahim, A Allagui, “Real-time platform for controlling DC microgrid based standalone solar energy conversion system,” *2016 International Conference on Industrial Informatics and Computer Systems (CIICS)*, Sharjah, United Arab Emirates, 13-15 March 2016.